Igneous sills as a record of horizontal shortening: The San Rafael Sub-Volcanic Field, Utah

R.J. Walker[1], D. Healy[2], T.M. Kawanzaruwa[1], K.A. Wright[3], R.W. England[1], K.J.W. McCaffrey[4], A.A. Bubeck[1], T.L. Stephens[1], N.J.C. Farrell[2], T.G. Blenkinsop[5]

[1] Department of Geology, University of Leicester, Leicester, LE1 7RH, UK

[2] School of Geosciences, King's College, University of Aberdeen, Aberdeen, AB24 3UE, UK

[3] DONG E&P (UK) Ltd, 5 Howick Place, London SW1P 1WG, UK

[4] Department of Earth Sciences, Durham University, Durham, DH1 3LE, UK

[5] School of Earth & Ocean Sciences, Cardiff University, Cardiff, CF10 3AT, UK

Corresponding Author: rw175@le.ac.uk

ABSTRACT

Igneous sills can facilitate significant lateral magma transport in the crust, therefore it is important to constrain controls on their formation and propagation. Close spatial association between sills and dikes in layered (sedimentary) host rocks has led to a number of sill emplacement mechanisms that involve stress rotation related to layering; from horizontal extension and dike emplacement, to horizontal compression and sill emplacement. Here we use field observations in the San Rafael subvolcanic field (Utah, USA), on the Colorado Plateau, supported by mechanical modelling, to show that layering is not the dominant control in all cases of sill formation. We found no compelling evidence of large sills fed by dikes; all observed cases show that either dikes cut sills, or vice versa. Local sill contacts activate and follow host layer interfaces, but regionally, sills cut the stratigraphy at a low angle. The sills cut and are cut by reverse faults (1-3 m

displacement) and related fractures that accommodate horizontal shortening. Minor sill networks resemble extension vein meshes, and indicate that horizontal and inclined geometries were formed during coaxial horizontal shortening and vertical thickening. Although sills elsewhere may be related to mechanical layering during tectonic quiescence, our mechanical models show that the observed SRSVF geometries are favoured in the upper crust during mild horizontal shortening. We propose that sill geometry provides an indication of regional stress states during emplacement, and are not all sill geometry is a response to bedding. Constraining sill geometry may therefore present a useful tool in plate tectonic studies.

1. Introduction

Igneous sill complexes represent a significant volumetric contribution to upper crustal magma systems (e.g., Planke et al., 2005; Muirhead et al., 2011), and they can play an important role in basin development, petroleum system maturation, and greenhouse gas generation (e.g., Svensen et al., 2004). Although vertical igneous dikes are typically assumed as being the dominant subvolcanic supply route for effusive volcanism (e.g., Ebinger et al., 2008), recent studies have shown that sills can also act as an important regional transport network (e.g., Galland et al., 2007; Airoldi et al., 2011; Muirhead et al., 2011; Airoldi et al., 2016; Magee et al., 2016). Dikes are commonly inferred to represent magma-filled extension mode (mode I) cracks that accommodate crustal extension, with the dike plane forming parallel to the plane of minimum normal stress: the plane containing σ_1-σ_2 (in this paper stresses are reckoned positive when compressive, with $\sigma_1 \geq \sigma_2 \geq \sigma_3$). In contrast, sills require a σ_1-σ_2 plane that is approaching horizontal, with σ_3 (near-)vertical. Dikes and sills are commonly found in close spatial association, particularly in sedimentary basins, yet transitions are rarely observed, especially in terms of dikes feeding kilometer-scale sills (i.e., sills that are laterally continuous at the km-scale; see Valentine & Krogh (2006) and Eide et al. (2016) for possible examples of this).

The assumption that vertical dikes feed sills has important implications for emplacement mechanisms in that it requires the σ_1-σ_2 plane to rotate from vertical (dikes) to horizontal (sills). There are a number of models to explain this, including a level of neutral buoyancy (Francis, 1982), and various controls imposed by host mechanical layering (Gudmundsson, 2011; Schofield et al., 2012; Magee et al., 2016). Analogue injection models have not been able to reproduce a dike-fed sill solely as a function of the level of neutral buoyancy: in all cases, the dike ceases ascent, and begins lateral propagation in the vertical plane rather than flattening into a sill (e.g., Lister and Kerr, 1991). Most analogue models achieve a transition to sills using imposed mechanical layering (Kavanagh et al., 2006) in a hydrostatic stress state (i.e. $\sigma_1=\sigma_2=\sigma_3$), implying that sills are a consequence of intrusion into a sub-horizontally bedded or layered host rock stratigraphy (Galland et al., 2012). Layering is therefore considered the dominant cause of sill emplacement, with sills fed by dikes. It is commonly overlooked, however, that many dike and sill systems are emplaced within regions subjected to a regional tectonic stress, which can contribute to host rock failure, leading to specific geometries relative to the stress state. Models that account for tectonic stress show that it is possible to cause dike-to-sill transitions as a result of an applied horizontal shortening (e.g., Menand et al., 2010; Maccaferri et al., 2011), but these tectonic-origin models have not gained traction; in each case, layering is considered the dominant control, despite the homogenous host setup in both models.

Here we present remote sensing and field characterization of sills from the San Rafael Sub-Volcanic Field (SRSVF, Utah: **Fig. 1**). Contrary to previous interpretations (e.g., Richardson et al., 2015), we find no observable field evidence that the exposed dikes fed sills. Instead, cross-cutting relationships with dikes and tectonic faults suggest regional horizontal shortening during sill (and dike) emplacement. We use a mechanical, poroelastic model to show how tectonic compression,

and related distributed low angle structures (i.e., thrust faults and horizontal extension fractures) could promote and facilitate sill formation. Our model for sill emplacement does not require horizontal mechanical layering for sill formation; the main control on sill geometry is tectonic stress, which could operate in tandem with local stress perturbations.

2. BACKGROUND: OBSERVATIONS AND MODELS FOR SILL EMPLACEMENT

2.1 Natural Sills

Many natural sills are described as exploiting stratigraphic contacts. This is demonstrably true at the local scale (i.e. meter- to hundreds-of-meter-scale), particularly in terms of identified sill segments, lobes, or fingers, inferred to represent the early stages of sill propagation before formation of a through-going sheet intrusion (Thomson and Hutton, 2004; Schofield et al., 2012). However, at the regional scale (i.e. kilometer-scale) many sills are shown to gently climb through stratigraphy (e.g., the Great Whin Sill, northern Britain: Francis, 1982; see also Walker, 1993). Such transgressive sills are commonly compared to 3-D seismic interpretations of sills, and field examples of exhumed *saucer-shaped* sills which exhibit a flat inner region, and transgress or cut up through stratigraphy as a series of ramp and flat segments (e.g., the Golden Valley Sill, Karoo Basin, South Africa: Malthe-Sørenssen et al., 2004; Polteau et al., 2008; Schofield et al., 2010). It is important to note however that transgression can result from a number of mechanisms that occur ahead of the propagating sill tip, including: (1) intrusion of magma into pre-existing faults or fractures; (2) intrusion of magma into new fractures or faults induced by the propagating sill (Magee et al., 2015); or (3) intrusion of tectonic faults and/or fractures formed coeval with magmatism. Exposed transgressive segments therefore are not unique to saucer-shaped sills.

2.2. Analogue and Numerical Models of Sill Emplacement

Galland et al. (2015) present a detailed review of analogue modelling of intrusion emplacement hence only a brief synopsis is provided here. Most modelling of horizontal or transgressive sill emplacement involves injecting fluid vertically into the experimental apparatus, either directly from a tube in the apparatus base plate, or via injection into an imposed vertical crack. Most experiments aim to impede vertical dike emplacement to form a sill, either with an experimental set up using two layers of contrasting material stiffness (e.g., Kavanagh et al., 2006), or by using a porous mesh at a particular level, which reduces cohesion within the material (e.g., Galland, 2012). The experiments in both cases use a static apparatus, in that the rigid walls of the box do not exert a tectonic stress on the experiment; the system should involve low deviatoric stress (i.e. approaching a hydrostatic system). It has been inferred that these types of experiment replicate the natural system, in which intrusions are commonly observed within bedded sequences. However, some horizontal intrusions cut vertically-oriented host layering or foliation (e.g., the Traigh Bhan na Sgurra Sill, Isle of Mull, Scotland: Preston, 2006; Holness and Humphreys, 2003), challenging the requirement for sub-horizontal mechanical layering (e.g. bedding).

Models have produced sills from vertical injection into homogenous media (e.g., Wyrick et al., 2014), depending on the apparatus configuration: in cases where the apparatus lateral boundaries were unconfined, dike geometries were most common. Confining the sides of the model (i.e. placing the host rock analogue sand within a box) led to a fluid-pressure-controlled differential stress state, such that the volume introduced by intrusion led to the generation of a horizontal σ_1, causing σ_3 to switch to the axis that is unconfined (i.e. vertical). This mechanism was originally proposed by Anderson (1951), in which forceful injection of magma into the crust, as dikes, would lead to compression in the surrounding host rock, and eventually lead to stress rotation and sill emplacement.

125 Excess pore fluid pressure (i.e. suprahydrostatic pressure) has been used to explain intrusion at
126 depths greater than ~2 km, as an alternative to rigidity contrasts, or neutral buoyancy (e.g.,
127 Gressier et al., 2010). In such cases the pore fluid factor, λ_v (where $\lambda_v = P_f/\sigma_v$ - the pore fluid
128 pressure divided by the vertical stress) is inferred to equal or exceed lithostatic values ($\lambda_v = 1$ or λ_v
129 > 1 respectively), at very low differential stress. Gressier et al. (2010) applied this model to the
130 Neuquen Basin, Argentina, which represents a Mesozoic rift basin that has been inverted during
131 Aptian-to-present Andean compression (Cobbold & Rossello, 2003); the models did not involve
132 horizontal compression as a function of an applied contraction, and the intrusive sheet orientation
133 followed contrasting rheological properties of host layering, without which extension fractures
134 and sheet intrusions would have no preferred orientation.
135
136 Some analogue models use differential stress to simulate tectonic stress conditions. Galland et al.
137 (2007) modelled intrusion in a developing fold and thrust system, simulating a convergent plate
138 margin, in which intrusions formed as inclined sheets along, and parallel to, developing thrust
139 faults. It is important to recognise that although this model involved horizontal shortening, the
140 formation of thrust faults will have relieved stress within the host medium, and the intrusion
141 experiment was probably conducted during low deviatoric stress. Menand et al. (2010) applied
142 horizontal compression, inducing a vertical minimum compressive stress (σ_3), in which a dike to sill
143 transition was achieved. They concluded that because models did not achieve instantaneous
144 rotation from a dike to a sill, the results did not scale to their observations of natural systems and
145 as such, host rock mechanical layering would be required for sill emplacement. The model results
146 are supported by numerical simulations by Maccaferri et al., (2011), who showed that dike to sill
147 transition during shortening would occur vertically over a few kilometers. With these exceptions,
148 sills and dikes in the majority of cases, are inferred to represent periods of low deviatoric stress.
149 This inferred stress state fits with the assumption that dikes and sills will form in the σ_1-σ_2 plane,

150 and has led to most sheet intrusions being treated as extension fractures, and therefore
151 mechanically equivalent to joints.
152
153 **3. The San Rafael Sub-Volcanic Field, Utah, USA**
154 The SRSVF is located on the western margin of the Colorado Plateau; about 120 km from the Basin
155 and Range Province (**Fig. 1**). The area is host to several Laramide-age folds with the SRSVF lying
156 between the Waterpocket monocline and the San Rafael Swell (**Figs 1,2**). The Colorado Plateau has
157 seen little reorganization since around ~8 Ma (Burchfiel et al., 1992; Faulds et al., 2008), and the
158 SRSVF is generally considered to have been tectonically inactive since Laramide shortening. The
159 SRSVF comprises about 200 dikes, sills, and volcanic breccia bodies, which were emplaced into
160 lithified Jurassic sediments between 3.7 to 4.6 Ma, contemporaneously with mafic volcanism
161 along the nearby margin of the western Colorado Plateau (**Fig. 1**). The SRSVF crops out over an
162 area of about 1200 km^2, and occupies an observable elevation range of ~500 m, emplaced within
163 the upper 1 km of the crust (Gartner, 1986). The intruded country rocks at outcrop are Middle
164 Jurassic strata of the San Rafael Group, consisting of the Carmel Formation (limestones,
165 sandstones, siltstones and mudstones), Entrada Sandstone, and Curtis (sandstone, siltstones and
166 conglomerates) and Summerville (siltstones, mudstone and fine-sandstones) Formations, which
167 were deposited in shallow/near-shore marine, paralic, and aeolian environments (Gilluly, 1927;
168 Delaney and Gartner, 1995). The San Rafael Group represents deposition into a basin >100 million
169 km^2, with remnants covering most of the Colorado Plateau. The sills are in places composite
170 (basalt-syenite in composition; Gilluly, 1927), with the mafic rock similar in composition to dykes
171 in the SRSVF (Gilluly, 1927; Williams, 1983).
172
173 Intrusions in the SRSVF were mapped via remote sensing analysis of high-resolution aerial imagery
174 (~60 cm pixel resolution; National Agricultural Imagery Program for Emery, Sevier, and Wayne

175 Counties), and 1 m and 10 m resolution topographic data sets. Remote sensing was supported by
176 existing geological maps (Doelling, 2004) and by field characterisation during this study. Dikes
177 were identified by colour contrast in aerial imagery and manually picked remotely in ArcGIS™ for
178 spatial distributions and dike segment strikes (**Figs 2 and 3**). Delaney and Gartner (1997) provide a
179 very detailed analysis of dike geometry; only a short account is provided here. Sill top surfaces
180 were picked where possible, using the top contact between the sill and host rock evident in aerial
181 images; lines representing those top contacts were draped onto the digital elevation models to
182 provide constraints on regional-scale sill geometry (**Fig. 4**). Idealized surfaces were projected
183 through line segments for sill top contacts, from which plane attitudes were derived (**Fig. 4**).
184
185 **3.1 Dikes**
186 *3.1.1 Observations*
187 Dikes in the SRSVF comprise about 2200 observed segments within the Jurassic strata (**Figures 1-**
188 **3**). The segments are stepped in plan and section view but no clear systematic en echelon left or
189 right stepping is observed. Dike segments show a range of strikes, dominantly between NW-SE
190 and NNE-SSW, with the mean and modal strike of segments being NNW-SSE (**Fig. 2B**). Dikes
191 commonly intersect at a low angle (**Figs 2C,D** and **3B,D,E**), with the acute bisector oriented NNW-
192 SSE to N-S (e.g., **Fig. 2C,D**). Dikes generally dip steeply (>80°) to the east or west, and no
193 preferential dip direction was noted (see also Delaney and Gartner, 1997). Many dike margins
194 preserve breccia of the country rock, which appear to be sourced from the adjacent wall rock,
195 rather than from other parts of the stratigraphy.
196
197 Dike segments show a range of tip geometries, from tapered to blunt (**Fig. 3C**). In some cases
198 these steps appear to show a close spatial relationship with the sedimentary layering (e.g., **Fig.**
199 **3C**), although this is not always the case (**Fig. 3B**). In other cases, dikes show minor deflection

200 across host layers (**Fig. 3A**). We find no clear instances of dikes transitioning into sills, either at the
201 local (m-scale), or regional (km-scale) scale. Where dikes and sills are observed together, dikes cut
202 sills (e.g., **Figs 5 and 6C,D**) or sills cut dikes (e.g., **Fig 7A,D**).
203
204 *3.1.2 Summary and Interpretations*
205 Dikes observed at outcrop in the SRSVF are interpreted to represent the segmented peripheral
206 extremity of connected dikes at depth. The vertical and horizontal stepping shows no preferential
207 orientation and we infer that the stepping represents intrusion of fracture segments that formed
208 ahead of the main dike tip, similar to the propagation and linkage of segmented faults and veins in
209 layered materials (e.g., Crider and Peacock, 2004).
210
211 The range in dike strikes can be interpreted in three ways, which are not mutually exclusive: (1)
212 reactivation of existing joints; (2) rotation of the principal stress axes; and/or (3) intrusion during
213 tectonic extension. Models 1 and 2 can be rationalised best if considering the intrusions as
214 opening mode fractures. Model 3 does not require that the dikes be opening mode, allowing the
215 through-going dike to accommodate at least a minor component of shear. We infer that the acute
216 angle observed between intersecting dikes could be achieved if the maximum compressive stress
217 (σ_1) and minimum compressive stress (σ_3) are both horizontal; from **Fig. 2C and D**, σ_1 would be
218 oriented N-S, and σ_3 oriented E-W. This extension direction is consistent with the findings of
219 Delaney and Gartner (1997), who associated dike strikes in the SRSVF with the probable
220 reactivation of host rock joint systems in the underlying (Triassic) Glen Canyon Group, and
221 inferring emplacement during low horizontal deviatoric stress (i.e. invoking models 1 and 2
222 above). Dike emplacement in the SRSVF appears to have been via newly-formed fractures of intact
223 rock, and the acute angle of intersection between dikes suggests elevated differential stress (i.e.
224 greater than four times the tensile strength of the rock; Ramsay and Chester, 2004). Although it is

possible that dikes inherited their strikes from the underlying joint systems, it is unclear why low deviatoric stress would not favour intrusion of joint sets at the level of exposure, particularly when low deviatoric stress is considered important in facilitating principal stress rotation to form the sills (Richardson et al., 2015) by way of exploitation of bedding planes.

We infer that variations in rock properties through the host stratigraphy have caused local deflection during dike propagation, but this does not appear to have been sufficient to cause deflection from dikes to sills. It is possible that dikes cutting sills observed at outcrop represent the feeders for sills above that have since been eroded. Alternatively dikes may have fed sills for an initial period, followed by a return to magma flow through vertical conduits; the present study cannot support or preclude either possibility based on field observations alone.

3.2. Sills

3.2.1 Observations

The sills are observed dominantly within the Entrada (sandstones and siltstones), but notable exceptions within the Carmel (siltstones and mudstones) and Summerville (siltstones, mudstone, and fine-sandstones) Formations do occur (**Fig. 1C**). Sills that cut formation boundaries are also observed, such as the Cedar Mountain sills (Entrada and Summerville Formations) and the Last Chance and Little Black Mountain sills (Carmel and Entrada Formations). Sills vary in thickness from <10 cm to about 30 m, and display vertical transgressions as steps along outcrop (**Fig. 7E**), as well as sub-horizontal and inclined sections (**Fig. 7A**). For the purposes of simplifying description, we will refer to sills that are <1 m thick as *thin* sills; those that are >1 m thick are termed *thick* sills.

Thin sills form complex networks of horizontal to inclined (~1° to 25°) sheets that are laterally continuous at the tens-of-metre to hundred-metre scale (**Figs. 7B and 8**). Individual sheets show

abrupt steps (**Fig. 8A**) as well as flat and ramp geometries (**Fig. 8A**). Numerous localities show segmented sheets separated by relay zones (*cf.* the bridge structures of Hutton, 2009; **Figs. 7A and 8B,C**). Where dipping sills intersect, chilled contacts are observed, showing intrusion of the younger sill followed solidification of the earlier sill. Where thin sills cut vertical fractures, the fractures are not intruded (e.g., **Figs 7D and 8A**).

Thin sill networks are cut by thick sills (**Figs 7A and 9**). As with instances of thin sills cutting other thin sills (**Fig. 9C**), chilled contacts in the thick sill and/or breccia of the thin sills indicate multiple stages of intrusion (**Fig. 9B**). Thick sills show the same dip range as thin sills (i.e. 0° to 25°: **Figs 4 and 10**). Thick sills show large (>10 m) abrupt vertical steps (**Fig. 7E**) as well as overlaps in which sill tips are more tapered (**Fig. 6E, 7A**). No consistent stepping direction is noted, and no shear sense is inferred. Many thick sills show internal contacts as chilled margins, suggesting that some may represent multiple sills (**Figs 7 and 9**).

Although there are a number of locations where the sills are parallel to bedding (e.g., **Figs 6A,B,C, 7A, and 10A**) sill systems gently climb through the stratigraphy at a low angle: in the south of the SRSVF, sills dip generally northeast or southwest (**Figs 4B, 7, and 10**), and in the northern part of the area, sills dip generally northwest or southeast (**Fig. 4A and 6**), forming an acute angle about the horizontal plane (e.g., **Fig. 10A**). In some areas, and within the Entrada Formation, sandstones around the sills host deformation bands and thrust faults (low angle reverse faults), which in the south of the SRSVF, dip northeast or southwest (**Fig. 7, 10, and 11**). Inclined segments of sills are sub-parallel to reverse faults (**Figs 10E and 11D**), with the long-axis of sill steps oriented sub-parallel to the σ_2 axis derived for the reverse faults (**Fig. 10C inset**). Key localities show that sills have intruded thrust-parallel fractures (**Fig. 11A,B,D,E**), but breccia of sills within fault rock,

gypsum veins that display dip-slip reverse motion, and low angle fractures within the sills, show that they are also cut by the faults (**Fig. 11B,F**).

3.1.1 Summary and Interpretations

Sills cross cut the bedding at a low angle. Shallowly-dipping mechanical discontinuities, such as bedding interfaces, faults, fractures, veins, and deformation bands have been intruded, whereas subvertical and vertical structures (fractures, faults, and joints; e.g. **Fig. 7A,B,D**) have not. In several key localities, linked sills are aligned parallel to reverse faults, and are cut by reverse faults (**Fig. 11**), suggesting that they were emplaced during horizontal shortening (**Fig. 10C inset**). The apparent bimodal to quadrimodal sill dip distribution is consistent with horizontal shortening either as a plane strain or during radial horizontal shortening respectively. The inclined sill segments do not occur towards the periphery of large sills, but rather occur at all scales: the SRSVF sills are not saucer shaped. Steps in the sills are sub-vertical, and show direct upward offset of the stratigraphy: the sills in almost all instances are accommodated by a relative vertical uplift of the sill roof (**Figs 7E, 10E, 11D**). Relative uplift of the roof is therefore accommodated by shear offset at inclined sill segments, rather than pure opening mode. Vertical fractures were not intruded, suggesting stress in the horizontal plane exceeds the magmatic pressure on the fracture plane. As shown in **Figure 10E**, some sills show a possible shear offset across the margins, which cannot be associated with an original thrust offset. In cases where the sills are horizontal, vertical opening represents an opening mode displacement (i.e. mode I extension), but for inclined sheets, vertical opening requires a component of shear offset (i.e. mixed mode opening). The opening direction is important as it suggests that the σ_3 axis was vertical in all cases; if all sills – inclined and horizontal – were purely opening mode, the σ_3 axis would have been inferred to rotate. Sills consistently dip in opposite directions – northeast and southwest, or northwest and southeast – respectively in the southern and northern parts of the SRSVF (**Fig. 4**). The σ_3 axis for these areas is inferred to be

299 coaxial, and the mutual cross-cutting relationship between minor sills with opposing dips, suggests
300 that they represent conjugate structures, with the σ_3 axis lying in the obtuse angle (**Fig. 12**).
301 Because vertical structures are not intruded during sill emplacement (note that it is been
302 established in section 3.1 that dikes and sills are cross-cutting) we can infer that the σ_1 and σ_2 axes
303 are horizontal *and* greater than the vertical σ_3; i.e. that σ_2 is not equal to σ_3 and that σ_2 probably
304 exceeded the magma pressure.
305
306 Analogue models have shown that dike and sill intrusion can cause deformation of the host rock,
307 and in particular, that inclined sills may cause reverse-sense offsets within the host medium (e.g.,
308 Wyrick et al., 2014). These models involve dike and sill emplacement in which the magma pressure
309 and magma volume drives differential stress and failure. It is possible that the reverse faults
310 observed in the SRSVF emanate from intrusions that are not observed, however, it is noted that in
311 cases with exceptional exposure around thick sills (e.g., the Last Chance and Cedar Mountain sills),
312 no reverse faults of this kind are observed. In addition, where observed, the majority of dikes are
313 later than the sills; Delaney and Gartner (1997) showed that in total, dikes in the SRSVF
314 accommodated ~17 m of E-W extension, hence at the time of sill emplacement, volume change
315 related to dikes is inferred to be minor.
316
317 **4. A NEW MODEL FOR SILL EMPLACEMENT: INTRUSION DURING HORIZONTAL SHORTENING**
318 **4.1. Conceptual model**
319 The SRSVF has been associated previously with dike emplacement accommodating ENE-WSW
320 extension during a period of low deviatoric stress (Delaney and Gartner, 1997). Low deviatoric
321 stress is important in their model, because it facilitates a range of dike strikes via activation of
322 joints in the host rock, and during phases of elevated magma pressure (i.e. where the magma
323 pressure exceeds the vertical principal stress) allows intrusion of sills along weak unit interfaces.

We have shown that sills intrude along bedding locally, but predominantly are at a low angle to it. The sills also show mutual cross cutting relationships with reverse faults, and do not intrude vertical fractures, suggesting that sills were emplaced at a time of horizontal shortening. Although sills have been shown previously in contractional settings (e.g. Galland et al., 2007; Tibaldi, 2008; Tibaldi, 2015), our descriptions represent an account of sills formed during tectonic contraction in a region that is generally considered tectonically inactive (Faulds et al., 2008), and adjacent to a major extensional province (the Basin and Range Province). Based on the close relationship between contractional faults and sills, we infer a propagation and inflation model for sill emplacement, similar to that presented by Walker (2016) for the Faroe Islands, on the NE Atlantic passive margin: (1) Regional compression, with a horizontal σ_1-σ_2 plane, and vertical σ_3 axis, resulted in the formation of distributed horizontal extension cracks (mode I) parallel to the σ_1-σ_2 plane, and localized thrust faults at a low angle to it (**Fig. 12a**); (2) magmatic activity resulted in local reactivation of preferentially-oriented pre-existing low-cohesion structures (i.e. those at a low angle to the σ_1-σ_2 plane), such as distributed microfractures, thrust faults, and lithological unit interfaces (**Fig. 12b**); and (3) inflation of individual segments, linked to create a through-going sill (**Fig. 12c-d)**. In this model, intrusions climb through stratigraphy at a low angle to the σ_1-σ_2 plane, but must also propagate laterally along the σ_2 axis. Magmatic inflation of segments is only possible where fractures become linked to the magmatic source (e.g., **Fig. 12b**). Sill propagation and magma flow may therefore be upward or downward, to link fractures in the vertical plane, and may also be horizontal, to link segments laterally. Our model differs from existing models for sill emplacement in two ways: (1) if present, layering serves as a local control only, and critically, is not *necessary* for horizontal intrusion; and (2) sills do not strictly need to form in the σ_1-σ_2 plane, but rather may form oblique to it overall; i.e. sills may not be magma-filled extension fractures, but rather magma-filled extensional-shear (or 'hybrid') faults. It is worth noting that under a horizontal compression imposed by tectonic stress, near-vertical faults and fractures may be

opened if the magma pressure has sufficient effect to overcome the normal stress on the plane. As no steeply-dipping faults, fractures, or joints in the host rock appear to be intruded (note it is important to distinguish between dilation or intrusion, versus slip along a structure to facilitate linkage of a horizontal sheet), we infer that the maximum and minimum compressive stress within the horizontal plane (SH_{max} and SH_{min} respectively) was greater than the effect of an applied magma pressure.

4.1. Mechanical model

4.1.1. Mechanical model background and parameters

Intrusions are generally viewed as fluid-filled fractures, in which the simplified stress state generally considered for intrusion as an extension fracture, is that the magma pressure (P_m) inside the fracture must exceed the least compressive stress (σ_3) plus the rock tensile strength (T) (Jaeger and Cook, 1979):

$$P_m > \sigma_3 + T \qquad \text{Equation (1)}$$

Extension (mode I) fractures are an end member form of brittle failure that do not involve shear-offset of the fracture walls. Inclined intrusions in the SRSVF show vertical opening, and therefore accommodate a minor component of shear. Extensional and contractional shear failure (mode II) is commonly simplified to the Mohr-Coulomb criterion for failure (**Fig. 13A**) which, taking into account fluid pressure, can be written as:

$$\tau_f = S + (\mu \sigma_n') \qquad \text{Equation (2)}$$

where τ_f is the shear stress at failure, S is shear cohesion, μ is the coefficient of internal friction for intact rock, and σ_n' is the effective normal stress (i.e., the normal stress σ, minus the pore fluid pressure P_f: Terzaghi, 1943). In this model, pore fluid pressure and magma pressure (P_f and P_m respectively) would have essentially the same contribution to rock failure, although it should be noted that intrusion of hot magma will be via cracks, whereas pore fluid pressure gains can occur within the host rock primary pore space (Hubbert and Willis, 1957). Equations 1 and 2 assume isotropic poroelasticity, with the pore fluid, or magma, hosted within statistically spherical or equant pore space. Following Carroll (1979) and Chen & Nur (1992), Healy (2012) modelled the effect of changing the shape of the pore space, considered more generally as ellipsoidal cracks, to induce poroelastic anisotropy within the rock volume as observed around faults, within damage zones and fault cores. Healy (2012) showed that, depending on the crack density and the orientation of the cracks relative to the *in situ* stress, significant deviations from the isotropic response to changes in fluid pressure are predicted. Considering the close association of sills with faults in the SRSVF, and because the magma is not transmitted via the primary (intergranular) pore space, but rather via cracks, we apply this model here. For comparison, our models show the role of isotropic crack distribution (i.e. randomly oriented cracks) as well as for anisotropic crack distribution (i.e. parallel cracks). The anisotropic models involve cracks that are oriented in the horizontal plane. The crack density (ρ) is an important factor in the response of the rock to an applied stress (Healy, 2012), hence we show here the results for a crack density of 0.1 (10^5 one-centimeter-radius cracks per m^3) and 0.4 ($4x10^5$ one-centimeter-radius cracks per m^3).

For our illustrative mechanical models, we assume a depth of sill emplacement of ~1 km (see e.g. Richardson et al., 2015), giving a vertical lithostatic load ($\sigma_{v} = \sigma_3$) of 25 MPa. The tensile strength (T) of the sandstone host rock is overestimated at 10 MPa, and we apply a shear cohesion (S) of 2T = 20 MPa (**Fig. 13**). According to the classical theory of effective stress and brittle failure (e.g.,

Hubbert & Rubey, 1959; Sibson, 2003), if the differential stress ($\sigma_d = \sigma_1-\sigma_3$) induced by tectonic loading is ≤ 4T (i.e., 0 MPa < σ_d ≤ 40 MPa), extensional failure of an isotropic rock will be achieved by applying a magmatic fluid pressure (P_m) that overcomes the vertical stress plus the tensile strength of intact rock: here P_m would need to be ≥35 MPa (**Fig. 13B**). In a truly horizontal compressional stress state, this will result in a horizontal extension (mode I) fracture (**Fig. 13**). At higher differential stress (i.e., where σ_d > 40 MPa), fracturing can be achieved only by shear (mode II) failure of the host rock (**Fig. 13A**). However, the Hubbert and Rubey (1959) model assumes a number of important parameters in terms of the response of the rock to changes in stress; in particular, the material compressibility (Poisson's ratio (ν : the ratio of lateral strain to an applied axial strain) and the bulk modulus (the ratio of pressure increase to a decrease in volume). Additionally, following Nur & Byerlee (1971) the bulk modulus should be considered in terms of the total porous volume (K) and the bulk modulus of the solid components (K_s), as the Biot coefficient (α):

$$\alpha = 1- K/K_s \qquad \text{Equation (3)}$$

Equations 1 and 2, and the classical model of Hubbert and Rubey (1959), assume that the Biot coefficient is 1, hence α is not shown in Equations 1 or 2. Where α = 1, an applied fluid pressure of 35 MPa moves the Mohr circle by 35 MPa (i.e., **Fig. 13B**). Decreasing α towards 0 will decrease the effect such that, where α = 0, the fluid pressure would have no effect. Poisson's ratio is also often overlooked in the approach to brittle failure. Poisson's ratio for isotropic rocks lies between 0 < ν ≤ 0.5, ranging from the very compressible to the incompressible, respectively, with an assumed ν = 0.25 commonly applied. The classical model involves perfect incompressibility (i.e. ν = 0.5), and 35 MPa fluid pressure will move the Mohr circle by 35 MPa (**Fig. 13B**); decreasing ν will decrease the effect of an applied fluid pressure because more of the work done is for compression of the pore

423 space itself, without changing the shape of the rock. For many rocks, even those without an
424 obvious fabric, Poisson's ratio departs from the assumed value of $\nu = 0.25$. Well-cemented
425 cohesive sandstones, many limestones, and crystalline granites display $\nu \leq 0.25$. Weaker, less well
426 consolidated sedimentary rocks, coals, shales, and hydrothermally altered crystalline rocks often
427 have $\nu >> 0.25$ (Gercek, 2007).
428
429 *4.1.1. Mechanical model results*
430 In our models, we apply 25 MPa fluid pressure (i.e. $\lambda_\nu = 1.0$), which could be considered as the
431 pressure of a pore fluid in the host rock, or the magma pressure within a static (non-propagating)
432 crack. The value for fluid pressure is specifically low, to illustrate the approach to failure only, and
433 is substantially less than the required 35 MPa fluid pressure required for mode I failure in the
434 Hubbert and Rubey (1959) model. The starting value for differential stress is equivalent to 4T for
435 intact rock (i.e. $\sigma_d = 40$ MPa), which is probably lower than the differential stress implied by thrust
436 faults that are interpreted to be coeval with the sills. For comparison, we also performed tests to
437 simulate failure conditions as a function of elevated fluid pressure (**Table 1**).
438
439 Applying a fluid pressure increase of 25 MPa in isotropic rocks moves the Mohr circle towards the
440 failure envelope, but maintains a constant differential stress (**Figs 13B and 14**): the effect of fluid
441 pressure is equal in the σ_1 and σ_3 directions. For a compressible rock (e.g. $\nu = 0.11$), the fluid
442 pressure is only sufficient to initiate a re-shear of existing cohesion-less surfaces if the crack
443 density (ρ) is increased. In **Figure 14A** we can see that where $\rho = 0.4$, re-shear is possible on
444 structures that are within an angular range of 11-42° to the σ_1 axis. Less compressible rocks ($\nu =$
445 0.4) have a significant response to 25 MPa fluid pressure, with re-shear of pre-existing cohesion-
446 less structures possible within an angular range of 12-41° where $\rho = 0.1$, and 0-55° where $\rho = 0.4$
447 (**Fig. 14B**). The predicted increased dilatancy of the less compressible rock is important in

448 controlling reactivation of existing surfaces, but as anticipated, neither of the *isotropic* poroelastic
449 models predicts intact rock failure. Increasing fluid pressure to intact rock failure highlights the
450 importance of crack density and Poisson's ratio, requiring fluid pressure to exceed the classical
451 model prediction of 35 MPa in all cases. Rocks with low Poisson's ratio and low (isotropic) crack
452 density require significantly greater fluid pressure to cause failure, than rocks with high Poisson's
453 ratio and high crack density (**Table 1; Fig. 14**).
454
455 For rocks with patterns of parallel cracks (in this case, horizontal and aligned parallel to σ_1), shear
456 stress and effective normal stress both change within the intact rock, with increases in fluid
457 (magma) pressure (**Fig. 15A,B**): the fluid pressure has greater fracture surface area to act upon
458 normal to σ_3 than there is to counteract σ_1 (and σ_2). This manifests itself in the poroelastic
459 framework as a directionality in the values of α (now a 2nd rank tensor, **Table 1**), leading to an
460 increase in differential stress. **Figure 15A** shows the effective stress change induced by a 25 MPa
461 increase in fluid pressure for a host rock with ν = 0.11. As fluid pressure increases, the differential
462 stress increases, and the stress state is driven towards brittle shear failure (i.e. the shear failure
463 envelope), with re-shear possible on cohesion-less structures within an angular range of 13-40°
464 and 1-52° where ρ = 0.1 and ρ = 0.4 respectively. Failure of intact rock in this case is achieved at 75
465 MPa and 34 MPa for crack densities of 0.1 and 0.4 respectively, with the latter falling below the
466 classical model prediction. Failure is predicted within the contractional shear portion of the failure
467 envelope: i.e. a thrust fault, with planes forming at an ideal angle of 25° to the σ_1 axis. In **Figure**
468 **15B**, an alternative model is presented for a host rock with ν = 0.4. In this case applying 25 MPa
469 fluid pressure increases differential stress, but the effect is subdued compared to ν = 0.11. Re-
470 shear is possible within an angular range of 7-46° and 0-56° where ρ = 0.1 and ρ = 0.4 respectively.
471 Intact rock failure is achieved with fluid pressure at 55 MPa and 32 MPa where ρ = 0.1 and ρ = 0.4
472 respectively. Notably, the latter falls below the predicted 35 MPa required in the classical model.

473 Failure occurs within the hybrid portion of the envelope; extensional shear is predicted (Ramsey &
474 Chester, 2004) with planes forming at an ideal angle of 18° to the σ_1 axis (**Fig. 15B**).
475
476 *4.1.1. Mechanical model summary*
477 Our mechanical model results have two very significant implications for intrusions in general: (1)
478 decreasing the host rock Poisson's ratio leads to a lesser response of the rock, when increasing
479 fluid pressure; and (2) the failure plane, and therefore sills (and dikes), may not be parallel to the
480 σ_1-σ_2 plane. The role of host rock Poisson's ratio in facilitating sill emplacement is important: a
481 larger ratio of vertical ("lateral") strain to horizontal ("axial") strain for a horizontally applied load
482 in a compressional thrust fault regime will promote more dilatancy for magma to occupy. Sills may
483 not necessarily prefer weaker rocks (i.e., rocks of lower brittle strength), but they may
484 preferentially intrude those with elevated values of Poisson's ratio (i.e., those that are more
485 elastically compliant). In addition, even at low fracture densities, anisotropic poroelasticity will
486 promote a deviation from mode I fracture. Our models involve low differential stress initially, but
487 increases in fluid pressure will increase differential stress due to the directional variation in the
488 Biot coefficient (**Table 1**), promoting shear failure. This effect may be particularly important at
489 depth, where tectonically-driven differential stress may exceed our starting value of four times the
490 tensile strength of the rock, and even in the near surface (~1 km) as indicated by the presence of
491 minor thrust faults in the SRSVF.
492
493 These simple poroelastic models describe only the *approach to failure*. Brittle failure of rock, by
494 shear or extensional fracturing, includes processes and deformation mechanisms that are not well
495 modelled by poroelasticity, including cataclasis, pore collapse, and the coalescence of microcracks
496 into through-going fractures. However, we maintain that the approach to failure, i.e. the effective
497 stress path followed by the rock mass towards fracture formation or reactivation, is the critical

498 part of the wider process of sill emplacement that we seek to address. We have only explored a
499 few parameters (i.e. crack density, Poisson's ratio, and the Biot coefficient) that contribute to the
500 response of a rock to an applied stress, rather than a full sensitivity analysis for elastic parameters.
501
502 **5. DISCUSSION**
503 **5.1. Is layering the primary control on sill formation in the SRSVF?**
504 Sills in the SRSVF do activate layer interfaces (e.g., **Fig. 10A**), and our model like others before it,
505 shows that stiff materials will fail at lower applied stress than soft materials (Eisenstadt and
506 DePaor, 1987; Ferrill et al., 2016). Sills also appear to intrude pre-existing fractures and thrusts
507 (**Fig. 11**). Material properties, and existing discontinuities can have a strong control on the
508 positioning of intrusions, and their geometry (McCaffrey and Petford, 1997; Schofield et al., 2012).
509 It is important to recognize that this does not mean the layer interface, or existing discontinuity is
510 the cause of the sill in all cases. Dikes in the SRSVF are observed at the same stratigraphic level as
511 the sills - within the same host units - and show cross-cutting relationships indicating dikes and
512 sills are not connected. Perhaps the greatest physical and mechanical property contrast in the
513 observed sequence is that between the sills and the sedimentary host rocks: dikes cut sill contacts
514 without major deflection. Hence other factors must control the formation of the SRSVF sills.
515 Notably, the orientation of dikes, and concurrent emplacement of sills, has been inferred to relate
516 to low deviatoric stress, and activation of existing joint sets in the underlying strata (Delaney and
517 Gartner, 1997); we have not observed any clear instances of sills feeding dikes; vertical fractures
518 are not intruded via sills. Where dikes cross unit interfaces, and formation boundaries, they exhibit
519 minor deflections in dip and/or strike, indicating interaction with the host mechanical stratigraphy
520 (**Fig. 3**). There are a number of well-accepted models for sill emplacement that involve mechanical
521 stratigraphy, including stress barrier configurations (Gudmundsson, 2006), elastic mismatch
522 (Dundurs, 1969) or material toughness variation (Kavanagh et al., 2006), and Cook-Gordon

523 delamination (Cook et al., 1964). In each case, a dike propagates through layering before one of
524 the above mechanisms causes the σ_3 axis to rotate from horizontal to vertical. Each mechanism is
525 strongly dependent on the host rock mechanical variation, including the material toughness and
526 fracture toughness, elasticity, and strength (cohesion) of the interface. Each mechanism is
527 modelled typically in a hydrostatic stress state. Each mechanism is partly dependent on the dike
528 being opening mode, rather than accommodating shear. Although this is likely for a significant
529 proportion of natural dikes and sills, it is unreasonable to assume it in all cases (Walker, 1993).
530 Analogue model results suggest sills require mechanical layering, and this gains some traction
531 from the preponderance of sills in layered sedimentary basin settings. However, if layering is the
532 primary control on sill formation in the SRSVF, then all other parameters being equal, all dikes
533 should rotate when they reach the same material interfaces. It is well know that propagation at an
534 interface may not be possible if the driving pressure is insufficient, or if the principal stress axes
535 are not oriented favourably (e.g., Gudmundsson, 2011). Despite this, the inference that dikes feed
536 sills has become so embedded in the literature, that it is not required for studies to show that
537 material interfaces have low cohesion, or that materials on either side of the interface differ
538 significantly in their properties. Clear examples of dike to sill transitions are generally small scale,
539 with meter-thickness dikes deflecting into sills for a few meters before returning to the original
540 dike geometry (Gudmundsson, 2011). If this mechanism of instantaneous deflection is to operate
541 at larger scales – to feed sills that are laterally continuous for many kilometers – there must be a
542 favourable stress state: either σ_3 is regionally vertical, or intrusion is during a low deviatoric
543 ambient stress state. We suggest that the sill geometry and position within the stratigraphy is
544 therefore an indication of the ambient stress: sills that cut layering may relate to phases of
545 horizontal shortening, whereas strictly layer-parallel sills may reflect the dominance of material
546 anisotropy presumably during periods of low deviatoric regional (tectonic) stress.
547

548 In our model, sills in the SRSVF were intruded during horizontal shortening, associated with a
549 vertical σ_3 axis. It is not clear from field observations how the sills are fed from below; whether
550 this is via a complex arrangement of gently transgressive to inclined sheets, or via unobserved
551 dikes. If the latter, a stress rotation is required, though notably this could involve switching the σ_2
552 and σ_3 axes, with a constant horizontal σ_1 axis. Based on the numerical models by Maccaferri et
553 al., (2011) and the analogue models of Menand et al. (2010), we infer that this rotation would be
554 gradual, occurring vertically over the hundred-meter scale or greater. In either case, we should not
555 expect to see the vertical feeder dike at the same stratigraphic level; rather we would require a
556 larger cross section through the system, in which we would probably observe sills fed by inclined
557 sheets, in turn fed by dikes at depth.
558
559 **5.2. Mechanisms for shortening during sill emplacement**
560 Our field study and poroelastic models show that tectonic shortening during magmatism could
561 facilitate sill intrusion, with new failure planes predicted to form at a low angle to the horizontal σ_1
562 axis, and reactivation of fractures at a broad range of angles from the horizontal σ_1 axis. The
563 angular range of these reactivated fractures is dependent on magma pressure having sufficient
564 effect to counter the normal stress on the plane. The models do not *require* stress rotation due to
565 mechanical layering, but would be *aided* by variations in elastic properties through the sequence.
566 By increasing the differential stress, intrusion at low angles to σ_1 is possible even at very low
567 magma overpressures (i.e. approaching $\lambda_v = 1$). We infer here that the sills in the San Rafael Sub-
568 Volcanic Field are representative of large sill complexes in which the primary control for their
569 emplacement is horizontal shortening. This is distinctly at odds with existing conceptual models
570 for sill emplacement, in particular because horizontal shortening is not recorded in association
571 with regional sill complexes. Shortening in the SRSVF is minor, and reverse faults probably account
572 for <1% horizontal shortening at the scale of the study area; our models are elastic only, and

573 although they do not quantify strains, the elastic range would probably involve shortening on the
574 order of <1%. Many studies of sill geometry are based on 3-D seismic data (e.g. Magee et al.,
575 2016), and such minor shortening may not be visible owing to the resolution limits of seismic
576 imaging. However, our model can account for sub-horizontal intrusion into homogenous or even
577 vertically-layered materials, in that the geometry of the sills is predicted to be controlled primarily
578 by the stress state. For instance, the gently-dipping basaltic sills at Loch Scridain on Mull, Scotland,
579 intrude vertically bedded and foliated, metamorphosed sandstones and mudstones, as well as
580 horizontally bedded lavas (Preston, 2006; Holness and Humphreys, 2003). Such examples cannot
581 be explained by stress rotation due to layering, nor neutral buoyancy, as the sills are observed in
582 both the basement and cover sequences. Models for discontinuity reactivation would predict dike
583 emplacement in the vertically foliated basement rocks, and sill emplacement in the horizontally-
584 layered cover. In stark contrast, dikes are present in the cover and basement, and sills gently climb
585 with respect to the paleo-horizontal regardless of the host rock foliation.
586
587 The cause of horizontal shortening in the SRSVF remains unclear, and previous studies of the
588 intrusions have considered the region as generally tectonically inactive since the late Cenozoic.
589 The SRSVF is located towards the western margin of the Colorado Plateau, adjacent to the Basin
590 and Range province (**Fig. 1**). The region is host to several Laramide-age folds, which predate
591 intrusion by >30 million years. Laramide folding relates to northeast-southwest shortening in the
592 Colorado Plateau (Davis, 1978). Imbricate thrust faults have been identified previously in the
593 Cedar Mountain area of the San Rafael Swell (north of the SRSVF; **Fig. 1**), but these are associated
594 with Laramide shortening also (Neuhauser, 1988). Cenozoic deformation in the region is
595 dominated by Basin and Range extension, though this is largely outwith the Colorado Plateau,
596 which has seen little structural reorganization since ~8 Ma (Burchfiel et al., 1992; Faulds et al.,
597 2008). The Plateau has been subject to considerable uplift since the Late Cretaceous (Liu and

598 Gurnis, 2010), with numerous mechanisms proposed as to the cause. The plateau currently stands
599 at ~2 km, but with a notable bowl-shape such that the margins are elevated ~400 m above the
600 plateau interior (Hunt, 1956; van Wijk et al., 2010). Again, the cause of this uplift geometry is
601 debated, but probably relates to edge-driven convection following lithospheric rehydration (van
602 Wijk et al., 2010) and lithospheric down-warping (Levander et al., 2011) particularly during the late
603 Cenozoic. The distribution of Pliocene volcanism, and incision rates in the Grand Canyon, suggest
604 this style of differential uplift has been active since ~ 6 Ma. Late Cenozoic lower crustal
605 delamination and crustal thinning was focused south of the SRSVF, within the Grand Canyon
606 Section of the plateau, which coincides with active normal faults that have accommodated ~100 m
607 Myr^{-1} differential uplift of the plateau relative to the Basin and Range (Lavender et al., 2011). The
608 SRSVF coincides with the margin of a down-welling body at ~200 km depth (**Fig. 1**; Levander et al.,
609 2011). Differential uplift of a region that is host to numerous pre-existing major structures (i.e.,
610 the Laramide-age fault systems) could result in a complex stress state and local/regional geometric
611 reactivation. We speculate that such differential uplift could provide a mechanism for upper
612 crustal horizontal compression. In this case, the direction of maximum horizontal shortening
613 would be oriented with respect to the major structures that are reactivated. Sills in the northern
614 SRSVF dip northwest and southeast, perhaps corresponding to reactivation of the NW-dipping San
615 Rafael Swell fault system. In the southern part of the SRSVF, the sills dip northeast and southwest,
616 normal to the crest of Waterpocket monocline. To our knowledge, the examples of thrust faults
617 presented here are the first recorded for this area. It is clear however that further work is needed
618 to relate these structures to specific events.
619
620 Horizontal shortening is not typically recorded in association with sill emplacement in rift basins,
621 or passive margins (see Sundvoll et al. (1992) and Walker (2016) for rare exceptions). However, it
622 should be noted that tectonic compression in the sense of a horizontal σ_1 axis, is recorded in rift

623 basins by variably-oriented folds, strike-slip faults that are oblique to basin bounding normal
624 faults, and recent or present day focal mechanisms. For instance, Walker (2016) showed that sills
625 cutting Paleocene lavas in the Faroe Islands were emplaced during horizontal shortening on the
626 Atlantic margin. Although not directly dated, the sills are cut by fault sets dated by Roberts and
627 Walker (2016), which bracket the age of the sills to ~54-46 Ma. Pre-, syn- and post-breakup mild
628 contractional folds are observed along the Atlantic margins, including along the NE Atlantic margin
629 from Ireland, past the Faroes and UK, and through to Norway (e.g., Doré et al., 2008). The timing
630 of tectonic compression along the margin therefore overlaps the timing of sill emplacement in
631 those areas (e.g., Magee et al., 2014). Pre- and syn-break-up contraction may be accounted for by
632 various rift propagation models (e.g., Hey et al., 1980, and references therein). Post break-up
633 shortening on the margin is typically inferred to reflect ridge push effects, or elevated gravitational
634 potential energy induced by the combination of an upstanding continental interior, and the large
635 volume represented by Iceland (e.g., Cloetingh et al., 2008). Syn- to post-break-up conjugate
636 strike-slip faults in the Faroe Islands and Faroe-Shetland basin accommodated crustal extension at
637 a high angle to the developing continental margin, but also a horizontal shortening sub-parallel to
638 the margin (Walker et al., 2011). Dikes that are parallel to those conjugate strike slip faults also
639 record crustal extension, and with minor shear offset across the dike planes; as extensional shear
640 structures, they are interpreted to represent conjugate intrusions, generated by a horizontal σ_1
641 and σ_3. Walker et al. (2011) and Walker (2016) showed that the horizontal shortening direction
642 and inferred σ_1 axis for conjugate dikes and sills in the Faroe Islands was coaxial: E-W. Dikes
643 recorded N-S horizontal extension (parallel to the inferred σ_3 axis), with a vertical inferred σ_2, and
644 sills record vertical extension (parallel to the inferred σ_3 axis), with a horizontal and N-S inferred
645 σ_2. Focal mechanisms for recent and present day earthquakes in active oceanic and continental
646 rifts, volcanic flank rift systems, and passive margin settings show that stress orientations can be
647 highly variable spatially, and temporally, across or along the rift axis, recording combinations of

extensional, contractional and strike-slip events (e.g. Stein et al., 1979; Ebinger et al., 2008; Green et al., 2014; Lin and Okubo, 2016). In summary, we suggest that applying our tectonic shortening model to sills in rift systems - considering sill complexes as a record of the regional stress - will lead to a better understanding of the intrinsically fluctuating nature of stress in such systems.

6. Conclusions

Mutual cross-cutting relationships between thrust faults and igneous sills in the San Rafael Sub-Volcanic Field in Utah, provide evidence for sill emplacement during horizontal shortening in a tectonically inert or extensional system. We infer that horizontal compression due to tectonic shortening may be a requirement for some other regional-scale horizontal intrusions, even in regions otherwise considered dominantly extensional. As a record of the stress state, igneous sills could be used as a tool to constrain regional tectonics, such as phases of compression within basins or along passive continental margins. Mechanical models show that sill emplacement can be aided by the development of oriented microcracks related to the compressional stress state, particularly at a local scale, around pre-existing faults where the high density of existing microcracks will facilitate failure at lower magnitudes of fluid overpressure. Our model for horizontal intrusion does not require host rock mechanical layering, and can be applied to horizontal intrusions within non-layered, or vertically-layered media.

Acknowledgements

The authors would like to thank DONG E&P UK for funding in support of this study. The authors gratefully acknowledge helpful reviews by Nick Schofield and Graham Andrews, and additional commentary from Associate Editor Bernhard Grasemann. Many thanks to Craig Magee and Agust Gudmundsson, as well as two anonymous reviewers, for their extensive and helpful reviews at an earlier stage in preparation of this paper.

673

674 **FIGURES**

675 **Fig. 1. Location maps for the San Rafael Sub-Volcanic Field in Utah.** (**A**) Digital elevation Model for
676 Utah, showing major structural and depositional areas of the Colorado Plateau. Solid black line
677 shows province boundaries. Dashed black line is a region of lower-crustal delamination and
678 crustal thinning detailed in Levander et al. (2011); dashed white line is their outline of a
679 downwelling body at 200 km depth, estimated from body wave tomography. (**B**) Aerial imagery
680 for the San Rafael Sub-Volcanic Field (SRSVF) highlighting location and distribution of intrusive
681 bodies. (**C**) Geological map of the region of interest, showing relative positions of the Northern
682 (N.) and Southern (S.) SRSVF. Cen.: Cenozoic. Cret.: Cretaceous. FM: Formation. Mbr: Member.
683 **Fig. 2. Dike orientations in the SRSVF.** (**A**) Hill shaded digital elevation model of the SRSVF
684 showing dikes identified from aerial images. (**B**) Rose plots show dike orientations, separated by
685 geographic location, and combined. Interpreted aerial image of dikes in (**C**) the eastern and (**D**)
686 the western SRSVF showing the acute angular relationship between dike segments.
687 **Fig. 3. Field photographs of dikes hosted in the Entrada Formation, within the SRSVF.** (**A**) 1 m
688 thick dike cuts sandstone-siltstone units, and shows minor angular deflection from vertical
689 through the siltstone. (**B**) Segmented dikes show acute angular relationship (~23°) along strike.
690 Segments both cut and abut a thin (10-30 cm thick) mudstone that separates siltstones above
691 and below. (**C**) Dike segment abuts upper contact of a mudstone. Dike appears to be
692 continuous across the mudstone, but shows a pronounced thinning above the contact, and ~1
693 m lateral offset. (**D**) Steeply-dipping dikes butting sandstones and siltstones. (**D**) Steeply-dipping
694 dike segments show segmentation in plan, and section view. Segment tips correspond to unit
695 boundaries in section view, but no pre-existing discontinuity is noted in plan view.
696 **Fig. 4. Geometric analysis of thick sills in the SRSVF.** Hillshaded digital elevation models for (**A**)
697 the northern SRSVF and (**B**) the southern SRSVF. Models show extrapolated elevation data for

sill top contacts. Lower hemisphere stereographic projections show sill top contact polygon attitudes as great circles, and contoured poles to planes for each sill system named in A and B. See text for details.

Fig. 5. Examples of cross-cutting relationships between sills and dikes. (**A**) Segmented dikes cut sills in the southern SRSVF. (**B-C**) Dikes cut sills in the northern SRSVF. Note that the thick sills in B and C are not parallel to bedding. Note that in C, dike segments (outlined with white dashes) cut the sill upper and lower contacts, but appear to abut internal sill contacts. (D-F) "Co-magmatic conduit of Richardson et al., (2015). Dikes within the volcanic breccia body (dark grey) cut thin sills below the main thick sill (light grey) shown in D. Chilled margin surfaces are observed at the same leval as the thick sill, though no direct contact is observed. Black star represents a marker to tie images D, E, and F.

Fig. 6. The Cedar mountain sills, northern SRSVF. (**A**) Photo panorama showing the Lower, Central, and Upper Cedar Mountain sills. (**B-D**) Dike and volcanic breccia body cut the Central Cedar Mountain sill. (**C**) Breccia body is developed along vertical joints in the sill. (**D**) Dike cuts volcanic breccia body, and shows chilled margin contacts with the Central Cedar Mountain sill. (**E**) Central Cedar Mountain sill is segmented across an apparent relay structure. Relay structure is brecciated, and hosts minor (cm-thick) sills that are inclined relative to the main sill.

Fig. 7. Examples of sills in the SRSVF. (**A**) 30 m thick sills in the southern SRSVF, are gently inclined relative to the host stratigraphy (at ~3°) such that the upper sill is observed intersecting the Entrada-Carmel Formation boundary ~700 m to the SW of the photograph. Note right hand edge of A is oriented N-S; black star indicates a marker point linking A and E. Breached relay structures (*cf.* broken bridges, e.g. Hutton, 2009), which record early sill segments, consistently strike NW-SE. Star shows reference position for view shown in E. (**B**) Thin sills (10 cm to 1 m thick) occur in close proximity to thick sills. Some thin sills are parallel to deformation bands, whereas some are horizontal. (**C**) Intrusions range in dip, from horizontal to ~60°; here, steeply

inclined sheets are cut and offset by shallowly-dipping sills. (**D**) Thin and thick sills cut vertical dike. (**E**) Lower thick sill shows abrupt vertical steps along exposure, whereas upper thick sill does not, suggesting the lower sill may predate the upper. Note the position of the lower sill base contact relative to the Entrada-Carmel Formation boundary.

Fig. 8. Examples of thin sills in the SRSVF. (**A**) Multiple sill network comprising cm-thick sills. Sills are generally bedding parallel but display local ramp sections that dip NE and SW. (**B**) Some thin sills are segmented, and separated by apparent relay structures that are intruded by inclined sheets. (**C**) Relay structures occur at a range of scales, up to ~2 m separation. Individual sills are stacked to form a multiple sill. (**D**) Locally, sills cross-cut each other, indicating staged intrusion.

Fig. 9. Relationship between thin and thick sills. (**A**) Thin sills are stacked to form multiple sills. (**B**) Locally, thick sill lobes cut thin sill contacts, forming breccia of thin sills. Long-dash line marks the contact between the thick sill and thin sills. Short-dash line marks the boundary between dominantly intact thin sills, and brecciated thin sills. (**C**) The volume of thick sills appears to be accommodated by folding of the country rock, including the thin sills.

Fig. 10. Gently-dipping sills in the southern SRSVF. (**A**) Thick sills are locally parallel to host bedding, but otherwise gently climb through the stratigraphy. Sills dips are dominantly NE and SW, and form an acute angle about the horizontal plane. (**B**) Thick and thin sills show NE and SW dips. (**C-D**) Thin sills range in attitude from horizontal, to inclined (~20-25°). Lower hemisphere stereographic projection shows deformation bands and thrusts in the southern SRSVF. Sills are locally parallel to (**D**) bedding, and (**E**) deformation bands and thrust faults. Thick arrows in E show sill opening direction. Lower hemisphere stereographic projection shows poles to planes for thrust and deformation band data collected in the southern SRSVF, at localities shown in **Fig. 10** and **Fig. 11**. Deformation band data is contoured in grey.

Fig. 11. Relationship between sills and reverse faults. (**A-C**) Sills cut and are cut by a thrust fault. (**B**) A multiple sill is cut by an E-dipping thrust. In the upper right of the image, a separate thin

sill is observed along the fault plane, inferred as representing post fault intrusion. (**C**) View from the other side of the crag shown in A and B. Minor fractures parallel to the thrust are observed in the multiple sill. Breccia of the sill is developed along the main thrust, and along minor faults that are sub-parallel to it. (**D-F**) A thick sill that shows a ramp-flat-ramp geometry, parallel to reverse faults (dipping 25-45° NE) within the country rock. Thick arrows in D show sill opening direction. (**E-F**) Inclined sills appear to have intruded parallel to thrusts, suggesting they reactivate existing structure, but are also locally cut by thrusts. (**F**) Bedding-parallel sill is dragged into a reverse fault. The sill hosts gypsum-mineralized fractures. Fault rock along the reverse fault comprises breccia of the country rock and the sill. (G) Multiple sill appears to be offset across a thrust fault (dipping ~10°E). Note that the country rock in contact with the sill displays thermal alteration, with the exception of the zone along the thrust plane. (H) Along the fault plane, the sill displays mineralized dip slip fault surfaces, and a 5-10 cm thick zone of altered fault rock.

Fig. 12. Conceptual model for sill emplacement during compression. (**A**) Horizontal shortening produces a fault and fracture system comprising isolated inclined and flat segments. (**B**) Existing fractures are in-filled and inflated by magma and propagate as extension and extensional shear veins. (**C**) Adjacent sheets link to form a through-going sill. New fractures and faults continue to form during on-going compression. (**D**) Minor sills are abandoned in favour of the more thermally efficient main sill. Note that, as this process may operate across scales, the illustrated box widths may represent centimetres to hundreds of metres, provided there is fault/fracture connectivity in or out of the page. We purposefully do not show the model *feeder* system, as this is not observed in the field.

Fig. 13. Mohr diagrams depicting the poroelastic response to isotropic pores and oriented cracks, and to different values of host rock Poisson's ratio. (A) Example Mohr diagram (shear stress, τ, against normal stress, σ) showing the composite failure envelope for intact rock (solid

773 black line) plus the re-shear condition for a cohesion-less fault (dashed black line), and critical
774 stress circles for the three mesoscopic modes of failure. θ represents the angle between the
775 failure plane and the σ_1 axis; θ_s denotes the angular range where reactivation is possible; μ is
776 the coefficient of friction; ϕ_i is the angle of internal friction for intact rock; ϕ_s is the angle of
777 internal friction for re-shear of a cohesion-less fault. Values are idealised based on the Berea
778 sandstone (Healy, 2012). (B) The classical model for the application of fluid pressure (P_f) (after
779 Hubbert and Rubey, 1959). The model involves idealised values for rock compressibility (i.e.
780 Poisson's ratio) and the Biot coefficient, so that the applied fluid pressure has a 1:1 influence on
781 the normal stress.
782 **Fig. 14.** Mohr diagrams illustrating the poroelastic effect of crack density, and Poisson's ratio at (A)
783 0.11, and (B) 0.4. Cracks in the model are randomly oriented (i.e. isotropic). Black circles are the
784 normal stress before fluid pressure is applied; grey short-dashed circle shows the effect of an
785 increase of 25 MPa fluid pressure where ρ = 0.1; grey long dashed lines circle shows the effect
786 of 25 MPa fluid pressure where ρ = 0.4; red circle shows failure condition.
787 **Fig. 15.** Mohr diagrams illustrating the poroelastic effect of anisotropic crack density, and
788 Poisson's ratio at (A) 0.11, and (B) 0.4. Cracks in the models are horizontal. Black circles are the
789 normal stress before fluid pressure is applied; grey short-dashed circle shows the effect of +25
790 MPa fluid pressure where ρ = 0.1; grey long dashed lines circle shows the effect of +25 MPa
791 fluid pressure where ρ = 0.4; red circle shows failure condition. (C) Photograph shows example
792 of sills in the southern SRSVF, highlighting the range of sill attitudes observed in the field.
793 Notably the extension direction is ubiquitously vertical, parallel to our inferred σ3 axis.
794 **TABLES**
795 **Table 1.** Mechanical model parameters and results corresponding to Figures 13, 14, and 15. ν,
796 Poisson's ratio; ρ, crack density; α, Biot coefficient; σD, differential stress; θs, reshear angle; P,
797 fluid pressure; θ, failure plane of intact rock; λν, pore fluid factor.

REFERENCES

Airoldi, G., Muirhead, J.D., White, J.D.L., and Rowland, J.V., 2011, Emplacement of magma at shallow depth: Insights from field relationships at Allan Hills, south Victoria Land, East Antarctica: Antarctic Science, v. 23, p. 281–296 doi:10.1017/S0954102011000095.

Airoldi, G.M., Muirhead, J.D., Long, S.M., Zanella, E. and White, J.D., 2016. Flow dynamics in mid-Jurassic dikes and sills of the Ferrar large igneous province and implications for long-distance magma transport. *Tectonophysics*, *683*, pp.182-199.

Anderson, E. M. 1951. The dynamics of faulting and dyke formation with applications to Britain, Edinburgh Oliver and Boyd.

Burchfiel, B.C. and Lipman, P.W., 1992. The Cordilleran orogen: conterminous US (No. 1). Geological Society of Amer. Geological map of Utah (Utah Geological Survey)

Carroll, M.M., 1979. An effective stress law for anisotropic elastic deformation. *Journal of Geophysical Research: Solid Earth*, *84*(B13), pp.7510-7512.

Chen, Q., Nur, A. 1992. Pore fluid pressure effects in anisotropic rocks: mechanisms of induced seismicity and weak faults. Pure and Applied Geophysics, 139, 463–479.

Cloetingh, S., Beekman, F., Ziegler, P.A., Van Wees, J-D., Sokouts, D. 2008. Post-rift compressional reactivation potential of passive margins and extensional basins. *In*: Johnson, H., Doré, A. G., Gatliff, R.W., Holdsworth, R., Lundin, E.R. & Ritchie, J.D. (eds) The nature and origin of compression in passive margins. *Geological Society, London, Special Publications*, **306**, 27-70

Cobbold, P.R. and Rossello, E.A., 2003. Aptian to recent compressional deformation, foothills of the Neuquén Basin, Argentina. *Marine and Petroleum Geology*, *20*(5), pp.429-443.

Cook, J., Gordon, J.E., Evans, C.C. and Marsh, D.M., 1964, December. A mechanism for the control of crack propagation in all-brittle systems. In *Proceedings of the Royal Society of London A: Mathematical, Physical and Engineering Sciences* (Vol. 282, No. 1391, pp. 508-520). The Royal Society.

Crider, J. G. & Peacock, D. C. P. 2004. Initiation of brittle faults in the upper crust: a review of field observations. Journal of Structural Geology, 26, 691-707.

Davis, G.H., 1978. Monocline fold pattern of the Colorado Plateau. Geological Society of America Memoirs, 151, pp.215-234.

Delaney PT, Gartner AE, 1995. Physical processes of shallow mafic dyke emplacement near the San Rafael Swell. USGS Open File Report 95-491

Delaney, P.T. and Gartner, A.E., 1997. Physical processes of shallow mafic dike emplacement near the San Rafael Swell, Utah. *Geological Society of America Bulletin*, *109*(9), pp.1177-1192.

Doelling, H.H. and Kuehne, P., 2007. Interim geologic map of the east half of the Loa 30'× 60' quadrangle. Wayne, Garfield, and Emery Counties, Utah: Utah Geological Survey Open-File Report, 489, p.28.

Doré, A.G., Lundin, E.R., Kusznir, N.J., Pascal, C. 2008. Potential mechanisms for the genesis of Cenozoic domal structures on the NE Atlantic margin: pros, cons and some new ideas. *In*: Johnson, H., Doré, A. G., Gatliff, R.W., Holdsworth, R., Lundin, E.R. & Ritchie, J.D. (eds) The nature and origin of compression in passive margins. *Geological Society, London, Special Publications*, **306**, 1-26

Dundurs, J., 1969. Discussion:"Edge-bonded dissimilar orthogonal elastic wedges under normal and shear loading"(Bogy, DB, 1968, ASME J. Appl. Mech., 35, pp. 460–466). *Journal of applied mechanics*, *36*(3), pp.650-652.

Ebinger, CJ., Keir, D., Ayele, A., Calais, E., Wright, T.J., Belachew, M., Hammond, J.O.S., Campbell, E., Buck W.R. 2008. Capturing magma intrusion and faulting processes during continental rupture: seismicity of the Dabbahu (Afar) rift. *Geophys. J. Int.* 174, 1138–1152

Eisenstadt, G. and De Paor, D.G., 1987. Alternative model of thrust-fault propagation. *Geology*, *15*(7), pp.630-633.

Faulds, J.E., Howard, K.A. and Duebendorfer, E.M., 2008. Cenozoic evolution of the abrupt Colorado Plateau–Basin and Range boundary, northwest Arizona: A tale of three basins, immense lacustrine-evaporite deposits, and the nascent Colorado River. Field Guides, 11, pp.119-151.

Ferrill, D.A., Morris, A.P., Wigginton, S.S., Smart, K.J., McGinnis, R.N. and Lehrmann, D., 2016. Deciphering thrust fault nucleation and propagation and the importance of footwall synclines. *Journal of Structural Geology*, *85*, pp.1-11.

Francis, E.H., 1982. Magma and sediment – I. Emplacement mechanism of Late Carboniferous tholeiite sills in northern Britain. J. Geol. Soc. London. 139(1): 1-20.

Galland, O. 2012. Experimental modelling of ground deformation associated with shallow magma intrusions. EPSL 317-318: 145-156

Galland, O., Cobbold, P.R., de Bremond d'Ars, J., Hallot, E., 2007. Rise and emplacement of magma during horizontal shortening of the brittle crust: insights from experimental modeling. J. Geophys. Res. 112. doi:10.1029/2006JB004604.

Galland, O., Holohan, E., van Wyk de Vries, B., Burchardt, S., 2015. Laboratory modelling of volcano plumbing systems: a review. Advs in Volcanology.

Gartner AE. 1986. Geometry and emplacement history of a basaltic intrusive complex, San Rafael Swell and Capitol Reef areas, Utah: U.S. Geological Survey Open-File Report 86- 81, 112

Gercek, H. 2007. Poisson's ratio values for rocks. International Journal of Rock Mechanics and Mining Sciences 44, 1, 1–13

Gilluly J. 1927. Analcite diabase and related alkaline syenite from Utah: American Journal of Science, v. 14, p. 199–211.

Green, R.G., White, R.S. and Greenfield, T., 2014. Motion in the north Iceland volcanic rift zone accommodated by bookshelf faulting. *Nature Geoscience*, *7*(1), pp.29-33.

Gressier, J.B., Mourgues, R., Bodet, L., Matthieu, J.Y., Galland, O. and Cobbold, P., 2010. Control of pore fluid pressure on depth of emplacement of magmatic sills: An experimental approach. *Tectonophysics*, *489*(1), pp.1-13.

Gudmundsson, A., 2006. How local stresses control magma-chamber ruptures, dyke injections, and eruptions in composite volcanoes. *Earth-Science Reviews*, *79*(1), pp.1-31.

Gudmundsson, A., 2011. Deflection of dykes into sills at discontinuities and magma-chamber formation. *Tectonophysics*, *500*(1), pp.50-64.

Healy, D. 2012. Anisotropic poroelasticity and the response of faulted rock to changes in pore-fluid pressure. In: Healy, D., Butler, R. W. H., Shipton, Z. K. & Sibson, R. H. (eds) 2012. Faulting, Fracturing and Igneous Intrusion in the Earth's Crust. Geological Society, London, Special Publications, 367, 201–214. http://dx.doi.org/10.1144/SP367.14

Hey RN, Duennebier FK, Morgan WJ. 1980. Propagating rifts on mid-ocean ridges. J. Geophys. Res. 85. 3647-3658.

Holness M.B., Humphreys, M.C.S. 2003. The Traigh BhaÁn na SguÁ rra Sill, Isle of Mull: Flow Localization in a Major Magma Conduit. Journal of Petrology 44(11): 1961-1976

Hubbert, M.K., Rubey, W.W. 1959. Role of fluid pressure in mechanics of overthrust faulting. Geological Society of America Bulletin, 70, 167.

Hubbert, M.K. and Willis, D.G., 1972. Mechanics of hydraulic fracturing.

Hunt, C.B., 1969. Geologic history of the Colorado River. US Geological Survey Professional Paper, 669, pp.59-130.

Hutton, D.H.W., 2009. Insights into magmatism in volcanic margins: Bridge structures and a new mechanism of basic sill emplacement-Theron Mountains, Antarctica, in Schofield, N., Turner, J.P., Underhill, J. (eds), Petroleum Geoscience; 1 August 2009; v. 15; no. 3; p. 269-278; DOI:10.1144/1354-079309-841

Jaeger, J.C., Cook, N. G. W. 1979. Fundamentals of Rock Mechanics. Methuen, London

Kavanagh JL, Menand T, Sparks S. 2006. An experimental investigation of sill formation and propagation in layered elastic media. Earth and Panetary science Letters, 245. 799-813

Levander, A., Schmandt, B., Miller, M.S., Liu, K., Karlstrom, K.E., Crow, R.S., Lee, C.T. and Humphreys, E.D., 2011. Continuing Colorado plateau uplift by delamination-style convective lithospheric downwelling. Nature, 472(7344), pp.461-465.

Lin, G. and Okubo, P.G., 2016. A large refined catalog of earthquake relocations and focal mechanisms for the Island of Hawai'i and its seismotectonic implications. *Journal of Geophysical Research: Solid Earth*, *121*(7), pp.5031-5048.

Lister lR, Kerr RC. 1991 . Fluid-mechanical models of crack propagation and their application to magma transport in dykes. 1. Geophys. Res. 96: 1 0,049-77

Liu, L. and Gurnis, M., 2010. Dynamic subsidence and uplift of the Colorado Plateau. Geology, 38(7), pp.663-666.

Maccaferri, F., Bonafede, M. and Rivalta, E., 2011. A quantitative study of the mechanisms governing dike propagation, dike arrest and sill formation. Journal of Volcanology and Geothermal Research, 208(1), pp.39-50.

Magee, C., Jackson, C.L. and Schofield, N., 2014. Diachronous sub-volcanic intrusion along deep-water margins: insights from the Irish Rockall Basin. *Basin Research*, *26*(1), pp.85-105.

Magee, C., Maharaj, S.M., Wrona, T. and Jackson, C.A.L., 2015. Controls on the expression of igneous intrusions in seismic reflection data. *Geosphere*, *11*(4), pp.1024-1041.

Magee, C., Muirhead, J.D., Karvelas, A., Holford, S.P., Jackson, C.A., Bastow, I.D., Schofield, N., Stevenson, C.T., McLean, C., McCarthy, W. and Shtukert, O., 2016. Lateral magma flow in mafic sill complexes. Geosphere, 12(3), pp.809-841.

Malthe-Sørenssen, A., Planke, S., Svensen, H. Jamtveit, B. 2004. Formation of saucer-shaped sills. *In*: BreitKreuz, C. & Petford, N. (eds) *Physical Geology of High-Level Magmatic Systems*. Geological Society, London, Special Publications, **234**, 215–227.

McCaffrey, K.J.W. and Petford, N., 1997. Are granitic intrusions scale invariant?. *Journal of the Geological Society*, *154*(1), pp.1-4.

Menand, T., Daniels, K.A., Benghiat, P., 2010. Dyke propagation and sill formation in a compressive tectonic environment. J. Geophys. Res., 115, B08201, doi:10.1029/2009JB006791

Muirhead, J.D., Airoldi, G., Rowland, J.V., White, J.D.L. 2011. Interconnected sills and inclined sheet intrusions control shallow magma transport in the Ferrar large igneous province, Antarctica. GSA Bulletin. doi: 10.1130/B30455.1

Muirhead, J.D., Van Eaton, A.R., Re, G., White, J.D. and Ort, M.H., 2016. Monogenetic volcanoes fed by interconnected dikes and sills in the Hopi Buttes volcanic field, Navajo Nation, USA. *Bulletin of Volcanology*, *78*(2), pp.1-16.

Neuhauser, K.R., 1988. Sevier-age ramp-style thrust faults at Cedar mountain, northwestern San Rafael swell (Colorado Plateau), Emery County, Utah. Geology, 16(4), pp.299-302.

Nur, A., & Byerlee, J. 1971. An exact effective stress law for elastic deformation of rock with fluids. Journal of Geophysical Research, 76(26), pp 6414-6419.

Planke, S., Rasmussen, T., Rey, S.S. Myklebust, R. 2005. Seismic characteristics and distribution of volcanic intrusions and hydrothermal vent complexes in the Vøring and Møre basins. In: Dore, A. G. & Vining, B. A. (eds) Petroleum Geology: North-West Europe and Global Perspectives - Proceedings of the 6th Petroleum Geology Conference, 833–844

Polteau, S., Ferre, E.C., Planke, S., Neumann, E.R. Chevallier, L. 2008. How are saucer-shaped sills emplaced? Constraints from the Golden Valley Sill, South Africa. *J. Geophys. Res.*, 113, B12104.

Preston, R.J. 1996. The petrogenesis of the Loch Scridain Xenolithic Sill Complex, Isle of Mull. Ph.D. thesis, University of Glasgow.

Ramsey, J.M., Chester, F.M. 2004. Hybrid fracture and the transition from extension fracture to shear fracture Nature.

Randall, B.A.O., 1959. Intrusive phenomena of the Whin sill, east of the R. North Tyne. *Geological Magazine*, *96*(05), pp.385-392.

Richardson, J.A., Connor, C.B., Wetmore, P.H., Connor, L.J. and Gallant, E.A., 2015. Role of sills in the development of volcanic fields: Insights from lidar mapping surveys of the San Rafael Swell, Utah. *Geology*, *43*(11), pp.1023-1026.

Schofield, N., Stevenson, C. & Reston, T. 2010. Magma fingers and host rock fluidization in the

948 emplacement of sills. *Geology*, **38**, 63–66.
949 Schofield N, Brown DJ, Magee C, Stevenson CT, 2012. Sill morphology and comparison of brittle and non-
950 brittle emplacement mechanisms, Journal of the Geological Society of London
951 Sibson, 2003. Brittle-failure controls on maximum sustainable overpressure in different tectonic regimes
952 AAPG Bulletin 87, 6.
953 Stein, S., Sleep, N.H., Geller, R.J., Wang, S.C. and Kroeger, G.C., 1979. Earthquakes along the passive margin
954 of eastern Canada. *Geophysical Research Letters*, *6*(7), pp.537-540.
955 Sundvoll, B., Larsen, B.T. and Wandaas, B., 1992. Early magmatic phase in the Oslo Rift and its related stress
956 regime. *Tectonophysics*, *208*(1), pp.37-54.
957 Svensen H, Planke S, Malthe-Sørenssen A, Jamtveit B, Myklebust R, Rasmussen Eidem T, Rey SS. 2004.
958 Release of methane from a volcanic basin as a mechanism for initial Eocene global warming. *Nature*
959 *429*, 542-545
960 Terzaghi, K. 1943. Theoretical Soil Mechanics. John Wiley & Sons, New York.
961 Tibaldi, A., 2008. Contractional tectonics and magma paths in volcanoes. *Journal of Volcanology and*
962 *Geothermal Research*, *176*(2), pp.291-301.
963 Tibaldi, A., 2015. Structure of volcano plumbing systems: A review of multi-parametric effects. *Journal of*
964 *Volcanology and Geothermal Research*, *298*, pp.85-135.
965 Valentine, G.A. and Krogh, K.E., 2006. Emplacement of shallow dikes and sills beneath a small basaltic
966 volcanic center–The role of pre-existing structure (Paiute Ridge, southern Nevada, USA). *Earth and*
967 *Planetary Science Letters*, *246*(3), pp.217-230.
968 Van Wijk, J.W., Baldridge, W.S., Van Hunen, J., Goes, S., Aster, R., Coblentz, D.D., Grand, S.P. and Ni, J.,
969 2010. Small-scale convection at the edge of the Colorado Plateau: Implications for topography,
970 magmatism, and evolution of Proterozoic lithosphere. Geology, 38(7), pp.611-614.
971 Walker, G. P. L. 1993. Re-evaluation of inclined intrusive sheets and dykes in the Cuillins volcano, Isle of
972 Skye. In: Prtichard, H.M., Alabaster, T., Harris, N.B.W and Neary, C.R. Magmatic Processes and Plate
973 Tectonics. Geological Society Special Publication, No. 76, 489-497.
974 Walker, RJ. 2016. Controls on transgressive sill growth. Geology
975 Walker, R.J., Holdsworth, R.E., Imber, J., Ellis, D., 2011. Onshore evidence for progressive changes in rifting
976 directions during continental break-up in the NE Atlantic: Journal of the Geological Society, v. 168, p.
977 27-48.
978 Williams JD. 1983. The petrography and differentiation of a composite sill from the San Rafael Swell region,
979 Utah [M.S. thesis]: Tempe, Arizona State University, 123
980 Wyrick, D.Y., Morris, A.P., Todt, M.K. and Watson-Morris, M.J., 2015. Physical analogue modelling of
981 Martian dyke-induced deformation. Geological Society, London, Special Publications, 401(1), pp.395-
982 403.

Fig. 1
W: 103.5 mm
H: 89mm
(Full page width)

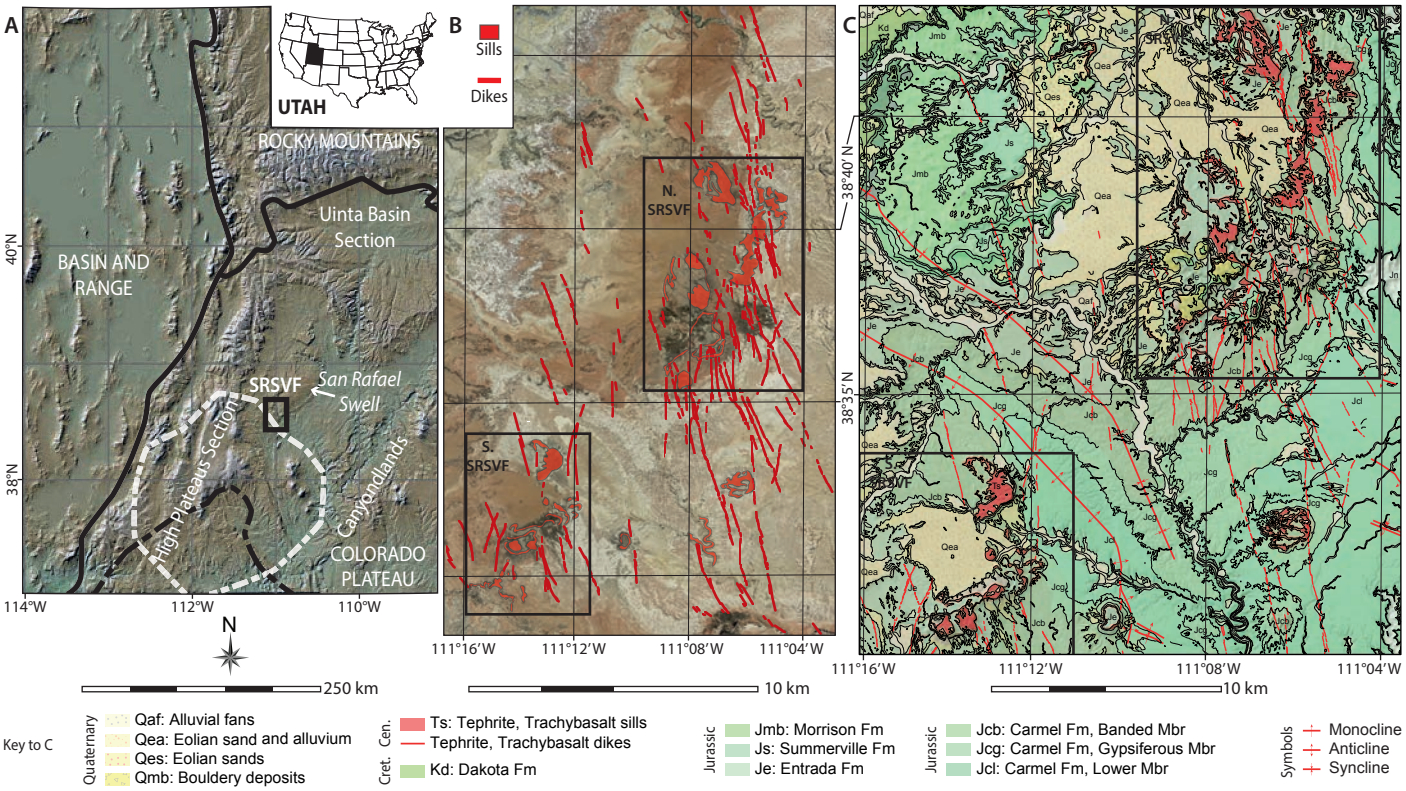

Fig. 1. Location maps for the San Rafael Sub-Volcanic Field in Utah. (A) Digital elevation Model for Utah, showing major structural and depositional areas of the Colorado Plateau. Solid black line shows province boundaries. Dashed black line is a region of lower-crustal delamination and crustal thinning detailed in Levander et al. (2011); dashed white line is their outline of a downwelling body at 200 km depth, estimated from body wave tomography. (B) Aerial imagery for the San Rafael Sub-Volcanic Field (SRSVF) highlighting location and distribution of intrusive bodies. (C) Geological map of the region of interest, showing relative positions of the Northern (N.) and Southern (S.) SRSVF. Cen.: Cenozoic. Cret.: Cretaceous. FM: Formation. Mbr: Member.

Fig. 2
W: 123 mm
H: 162 mm
(2-column width)

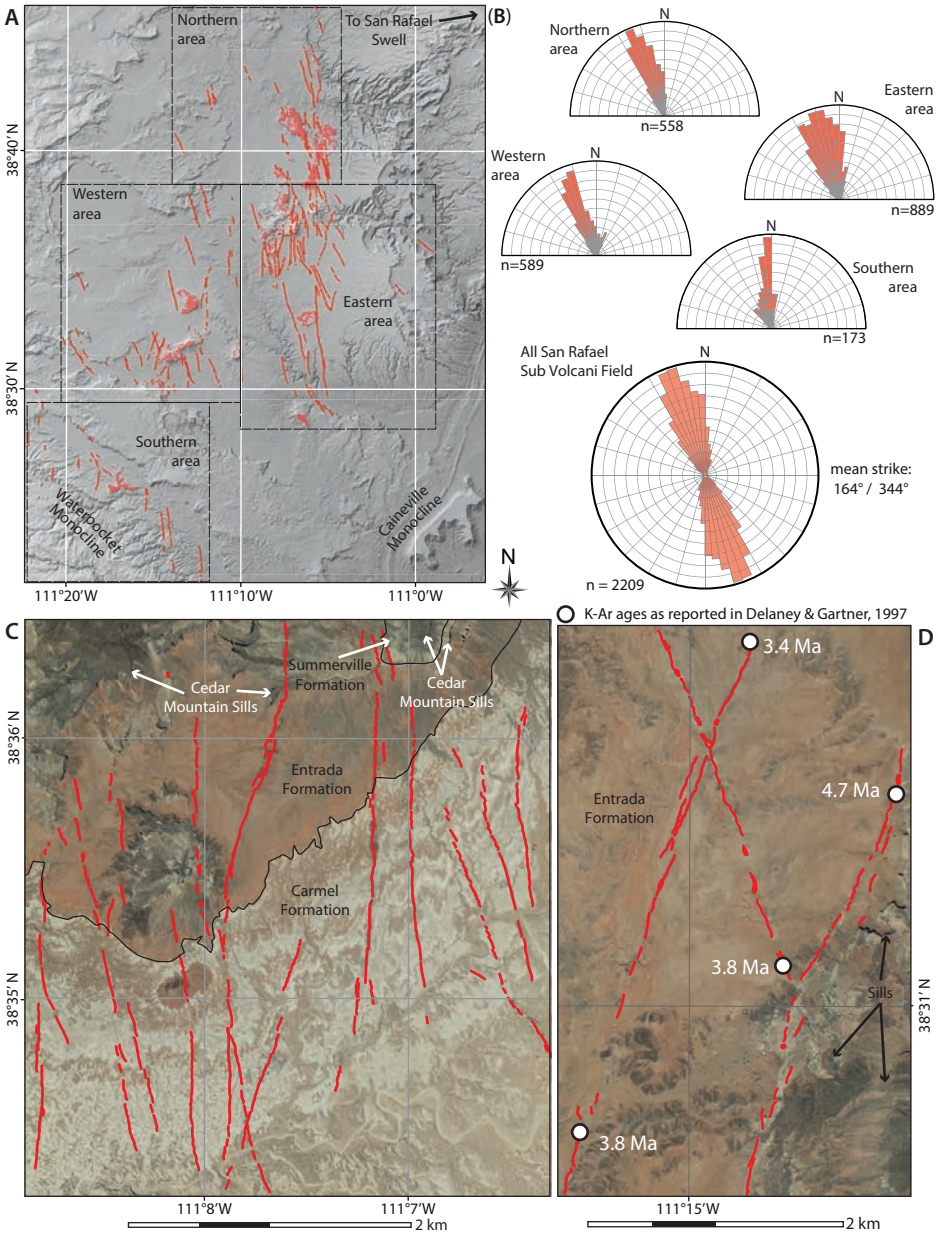

Fig. 2. Dike orientations in the SRSVF. (A) Hill shaded digital elevation model of the SRSVF showing dikes identified from aerial images. (B) Rose plots show dike orientations, separated by geographic location, and combined. Interpreted aerial image of dikes in (C) the eastern and (D) the western SRSVF showing the acute angular relationship between dike segments.

Fig. 3
W: 125 mm
H: 125 mm
(2-column width)

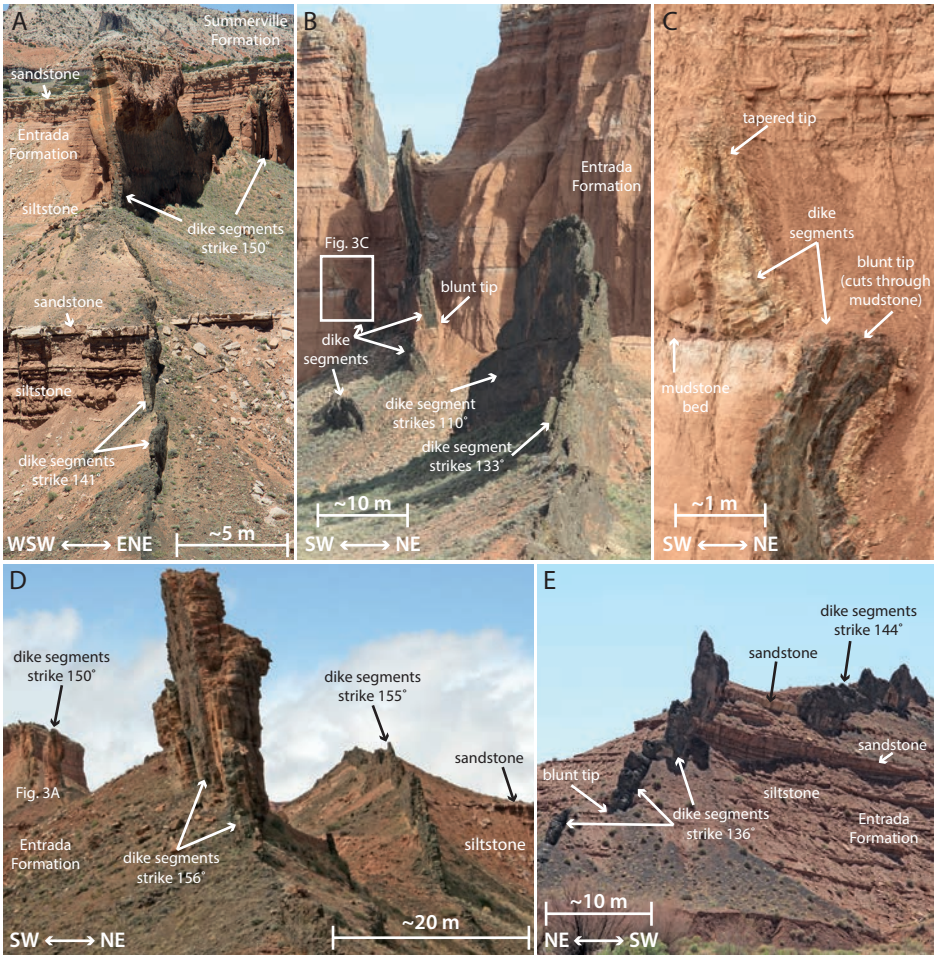

Fig. 3. Field photographs of dikes hosted in the Entrada Formation, within the SRSVF. (A) 1 m thick dike cuts sandstone-siltstone units, and shows minor angular deflection from vertical through the siltstone. (B) Segmented dikes show acute angular relationship (~23°) along strike. Segments both cut and abut a thin (10-30 cm thick) mudstone that separates siltstones above and below. (C) Dike segment abuts upper contact of a mudstone. Dike appears to be continuous across the mudstone, but shows a pronounced thinning above the contact, and ~1 m lateral offset. (D) Steeply-dipping dikes butting sandstones and siltstones. (D) Steeply-dipping dike segments show segmentation in plan, and section view. Segment tips correspond to unit boundaries in section view, but no pre-existing discontinuity is noted in plan view.

Fig. 4
W: 123 mm
H: 173 mm

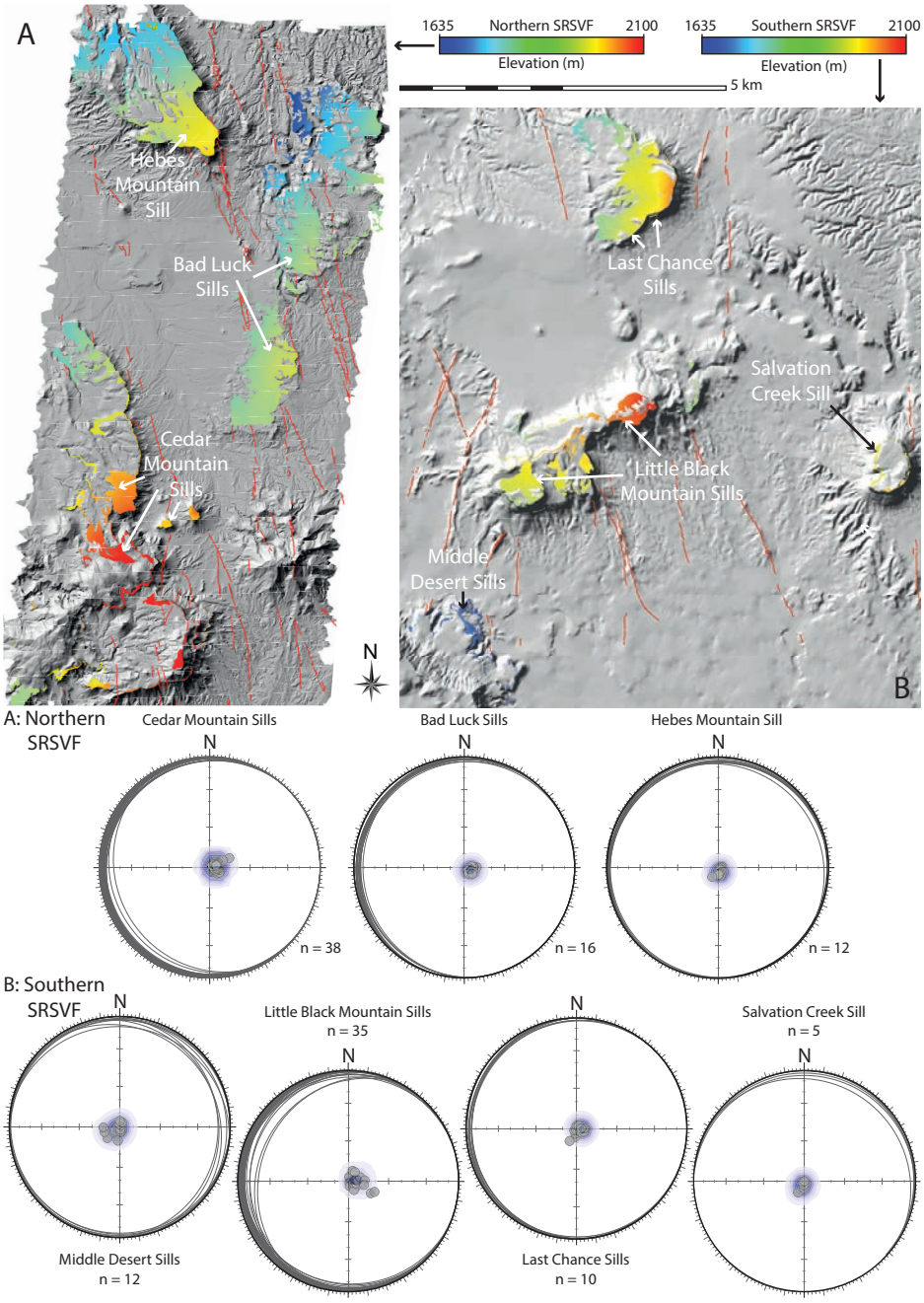

Fig. 4. Geometric analysis of thick sills in the SRSVF. Hillshaded digital elevation models for (A) the northern SRSVF and (B) the southern SRSVF. Models show extrapolated elevation data for sill top contacts. Lower hemisphere stereographic projections show sill top contact polygon attitudes as great circles, and contoured poles to planes for each sill system named in A and B. See text for details.

Fig. 5
w: 185 mm
H: 128 mm
(full page width)

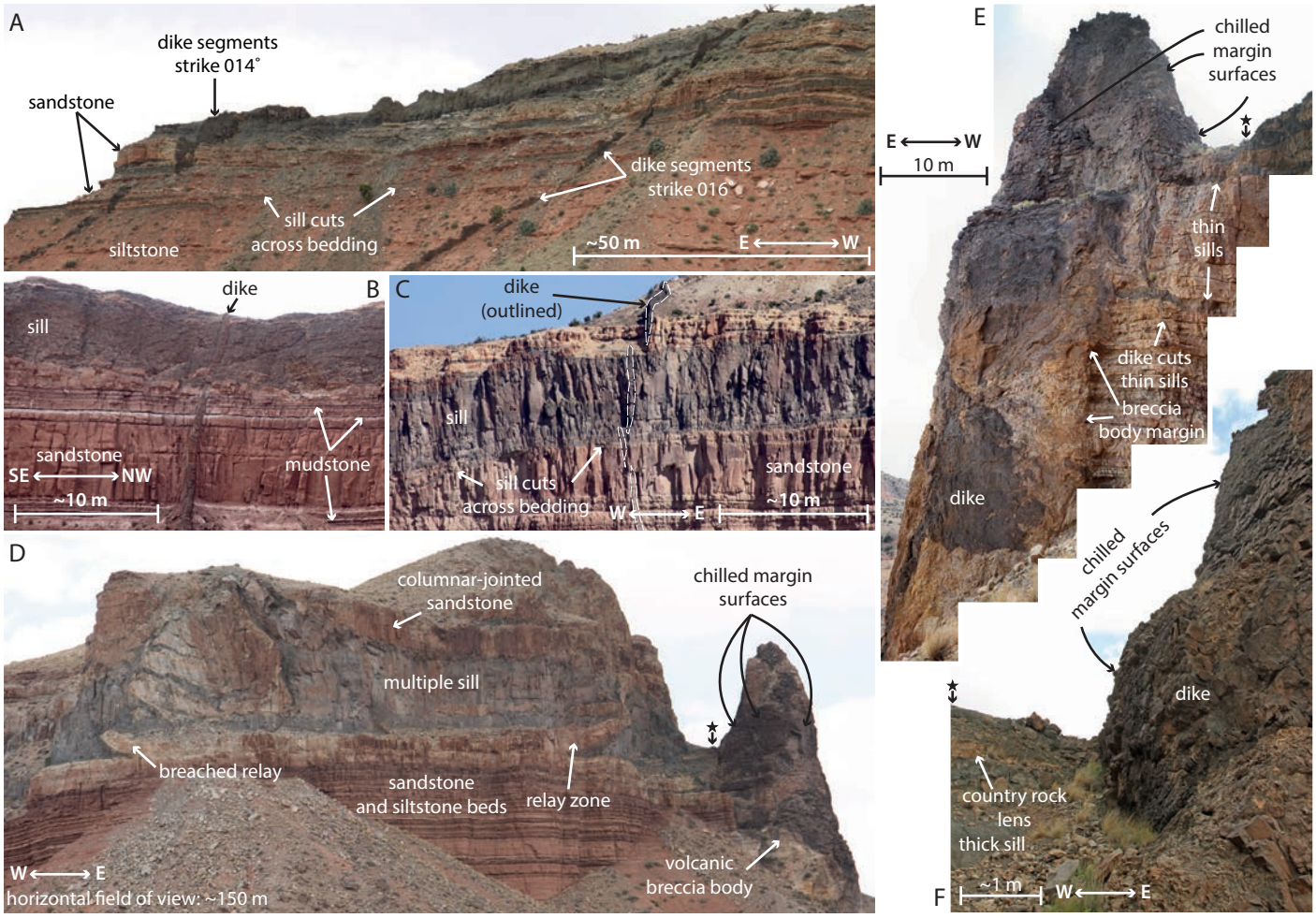

Fig. 5. Examples of cross-cutting relationships between sills and dikes. (A) Segmented dikes cut sills in the southern SRSVF. (B-C) Dikes cut sills in the northern SRSVF. Note that the thick sills in B and C are not parallel to bedding. Note that in C, dike segments (outlined with white dashes) cut the sill upper and lower contacts, but appear to abut internal sill contacts. (D-F) "Co-magmatic conduit of Richardson et al., (2015). Dikes within the volcanic breccia body (dark grey) cut thin sills below the main thick sill (light grey) shown in D. Chilled margin surfaces are observed at the same leval as the thick sill, though no direct contact is observed. Black star represents a marker to tie images D, E, and F.

Fig. 6
W: 185 mm
H: 197 mm
(Full page width)

Fig. 6. The Cedar mountain sills, northern SRSVF. (A) Photo panorama showing the Lower, Central, and Upper Cedar Mountain sills. (B-D) Dike and volcanic breccia body cut the Central Cedar Mountain sill. (C) Breccia body is developed along vertical joints in the sill. (D) Dike cuts volcanic breccia body, and shows chilled margin contacts with the Central Cedar Mountain sill. (E) Central Cedar Mountain sill is segmented across an apparent relay structure. Relay structure is brecciated, and hosts minor (cm-thick) sills that are inclined relative to the main sill.

Fig. 7
W: 225 mm
H: 112 mm
(2 column height, landscape)

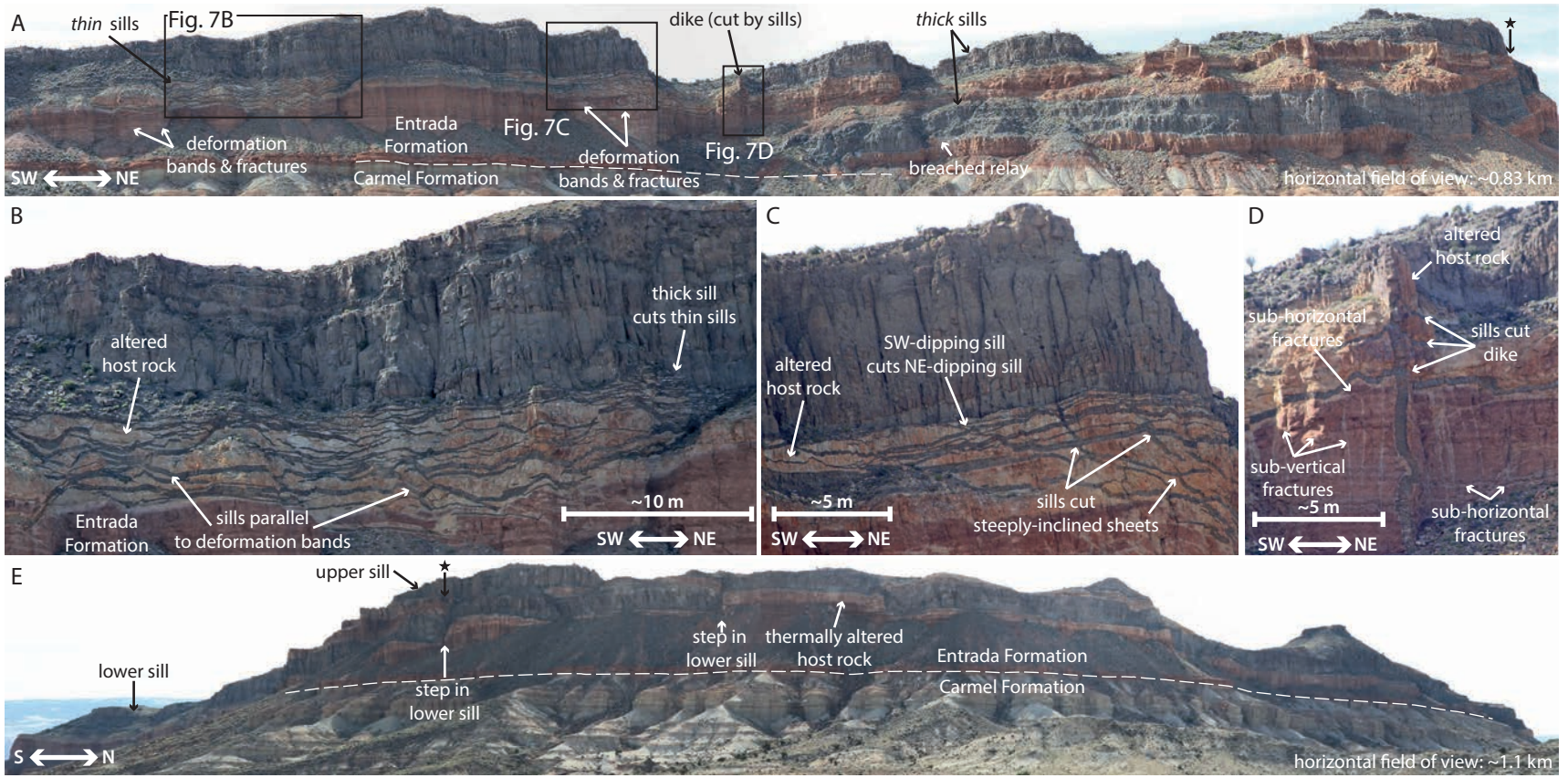

Fig. 7. Examples of sills in the SRSVF. (A) 30 m thick sills in the southern SRSVF, are gently inclined relative to the host stratigraphy (at ~3°) such that the upper sill is observed intersecting the Entrada-Carmel Formation boundary ~700 m to the SW of the photograph. Note right hand edge of A is oriented N-S; black star indicates a marker point linking A and E. Breached relay structures (cf. broken bridges, e.g. Hutton, 2009), which record early sill segments, consistently strike NW-SE. Star shows reference position for view shown in E. (B) Thin sills (10 cm to 1 m thick) occur in close proximity to thick sills. Some thin sills are parallel to deformation bands, whereas some are horizontal. (C) Intrusions range in dip, from horizontal to ~60°; here, steeply inclined sheets are cut and offset by shallowly-dipping sills. (D) Thin and thick sills cut vertical dike. (E) Lower thick sill shows abrupt vertical steps along exposure, whereas upper thick sill does not, suggesting the lower sill may predate the upper. Note the position of the lower sill base contact relative to the Entrada-Carmel Formation boundary.

Fig. 8
W: 185 mm
H: 83 mm
(Full page width)

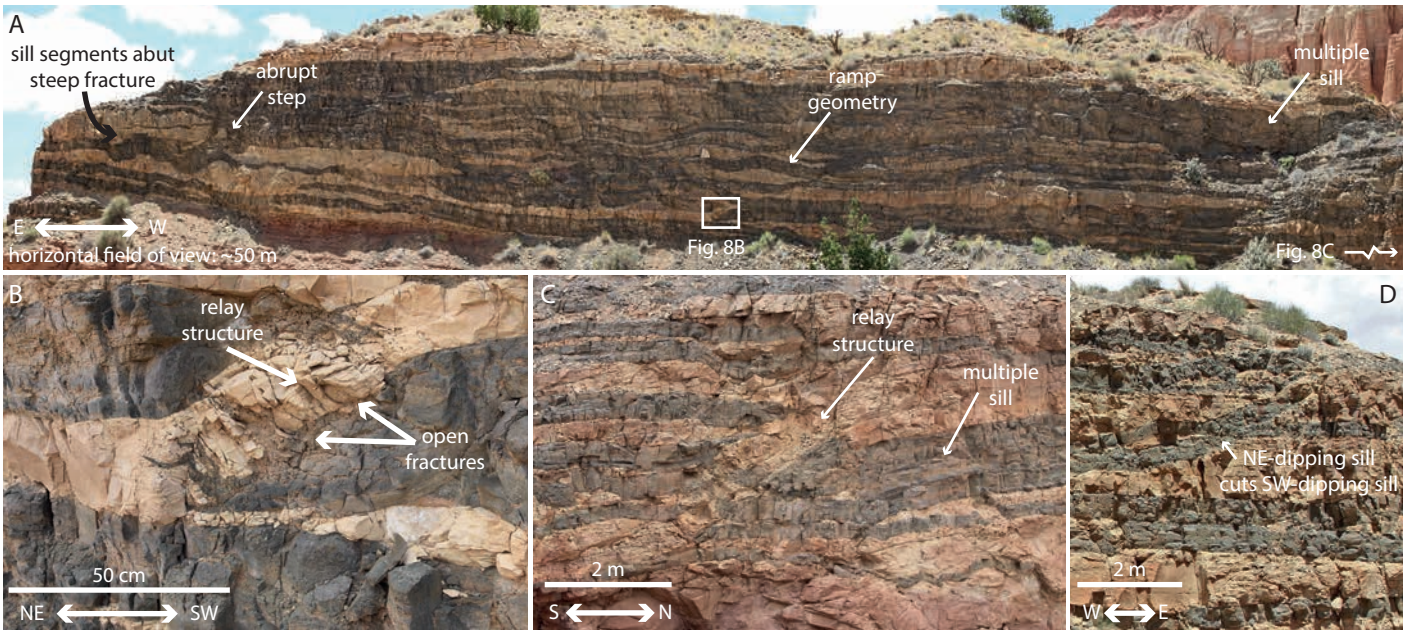

Fig. 8. Examples of thin sills in the SRSVF. (A) Multiple sill network comprising cm-thick sills. Sills are generally bedding parallel but display local ramp sections that dip NE and SW. (B) Some thin sills are segmented, and separated by apparent relay structures that are intruded by inclined sheets. (C) Relay structures occur at a range of scales, up to ~2 m separation. Individual sills are stacked to form a multiple sill. (D) Locally, sills cross-cut each other, indicating staged intrusion.

Fig. 9
W: 185 mm
H: 122 mm
(full page width)

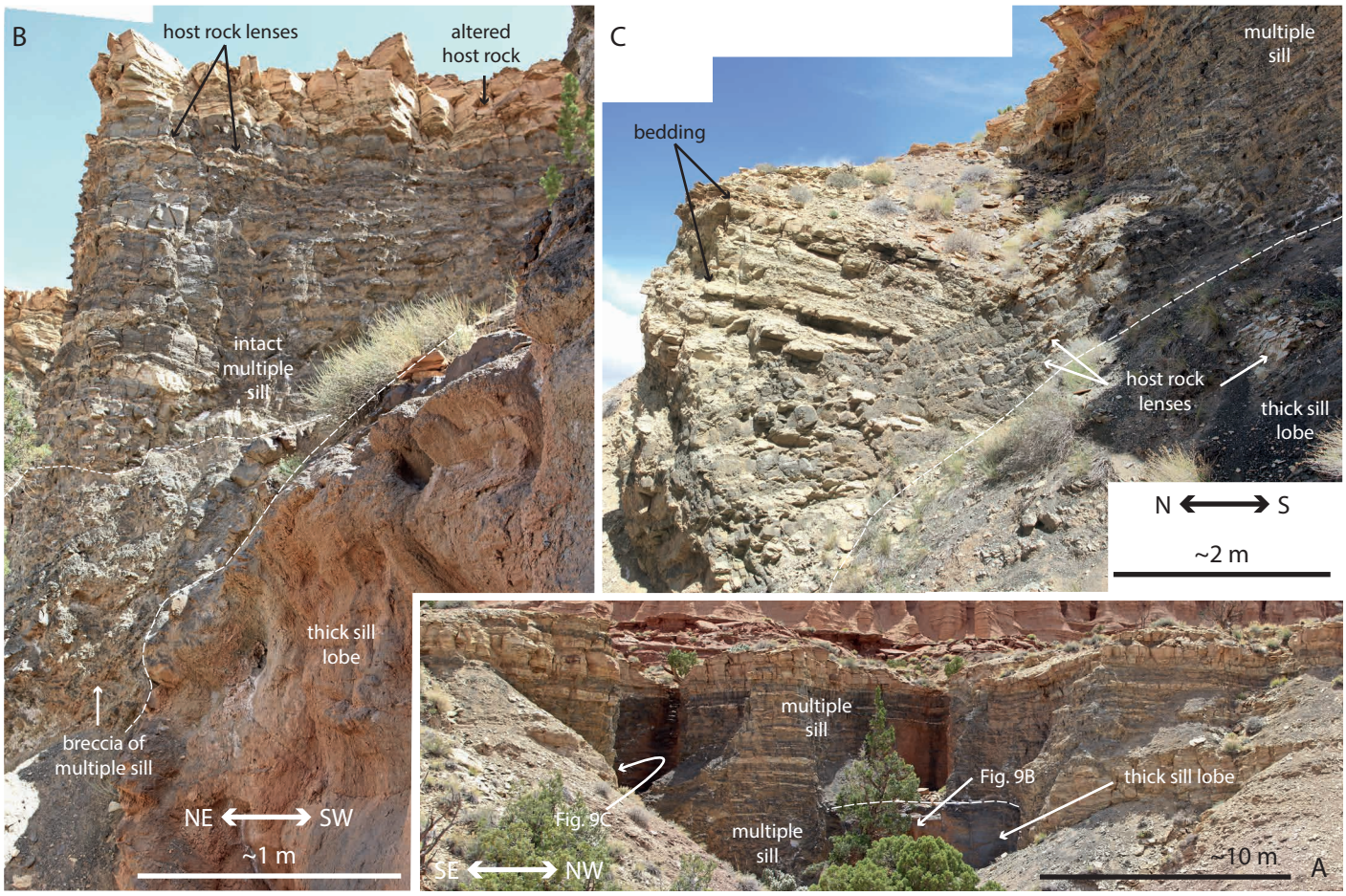

Fig. 9. Relationship between thin and thick sills. (A) Thin sills are stacked to form multiple sills. (B) Locally, thick sill lobes cut thin sill contacts, forming breccia of thin sills. Long-dash line marks the contact between the thick sill and thin sills. Short-dash line marks the boundary between dominantly intact thin sills, and brecciated thin sills. (C) The volume of thick sills appears to be accommodated by folding of the country rock, including the thin sills.

Fig. 10
W: 185 mm
H: 139 mm
(Full page width)

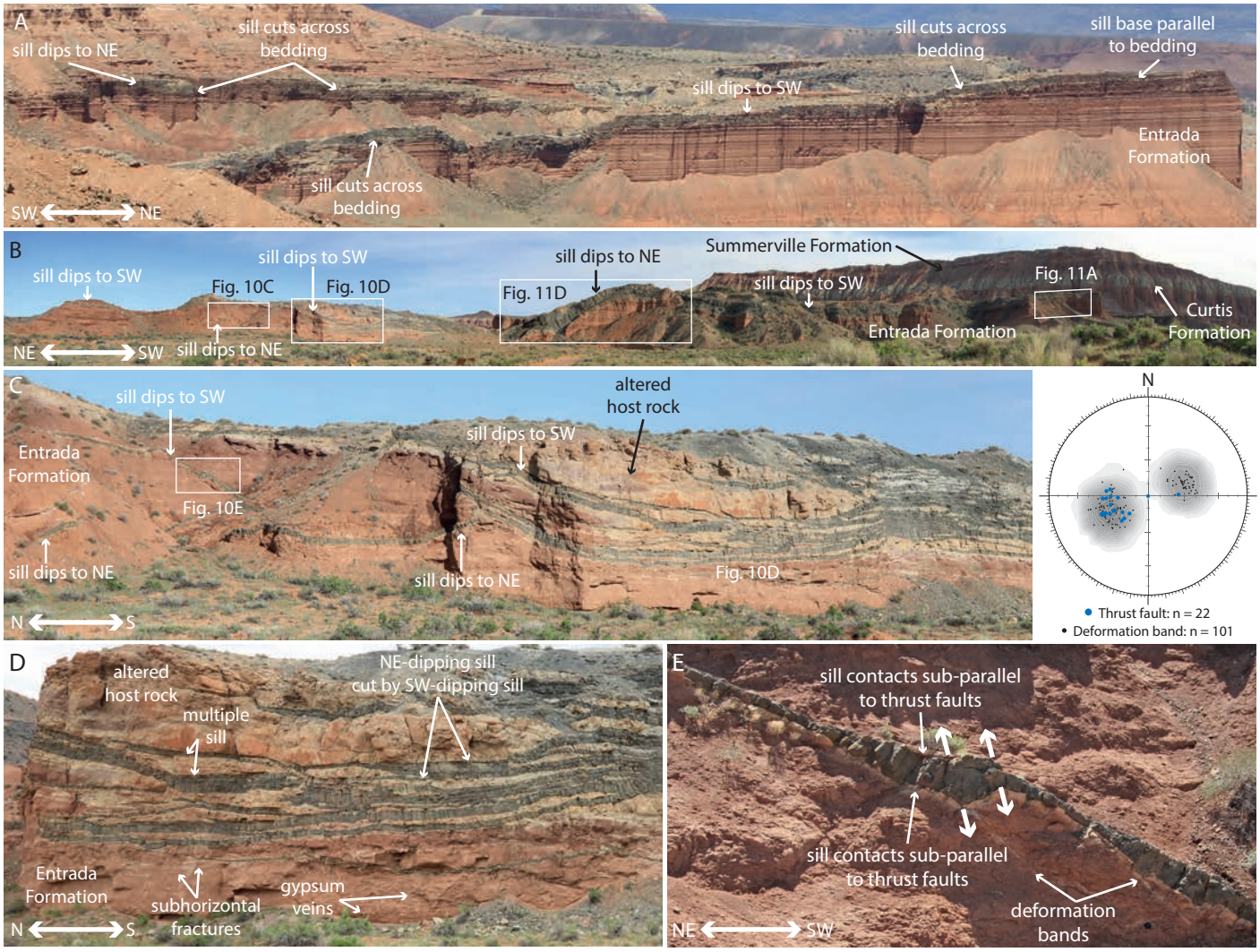

Fig. 10. Gently-dipping sills in the southern SRSVF. (A) Thick sills are locally parallel to host bedding, but otherwise gently climb through the stratigraphy. Sills dips are dominantly NE and SW, and form an acute angle about the horizontal plane. (B) Thick and thin sills show NE and SW dips. (C-D) Thin sills range in attitude from horizontal, to inclined (~20-25°). Lower hemisphere stereographic projection shows deformation bands and thrusts in the southern SRSVF. Sills are locally parallel to (D) bedding, and (E) deformation bands and thrust faults. Thick arrows in E show sill opening direction. Lower hemisphere stereographic projection shows poles to planes for thrust and deformation band data collected in the southern SRSVF, at localities shown in Fig. 10 and Fig. 11. Deformation band data is contoured in grey.

Fig. 11
W: 123 mm
H: 311 mm
(full page width; split to 2 pages for height)

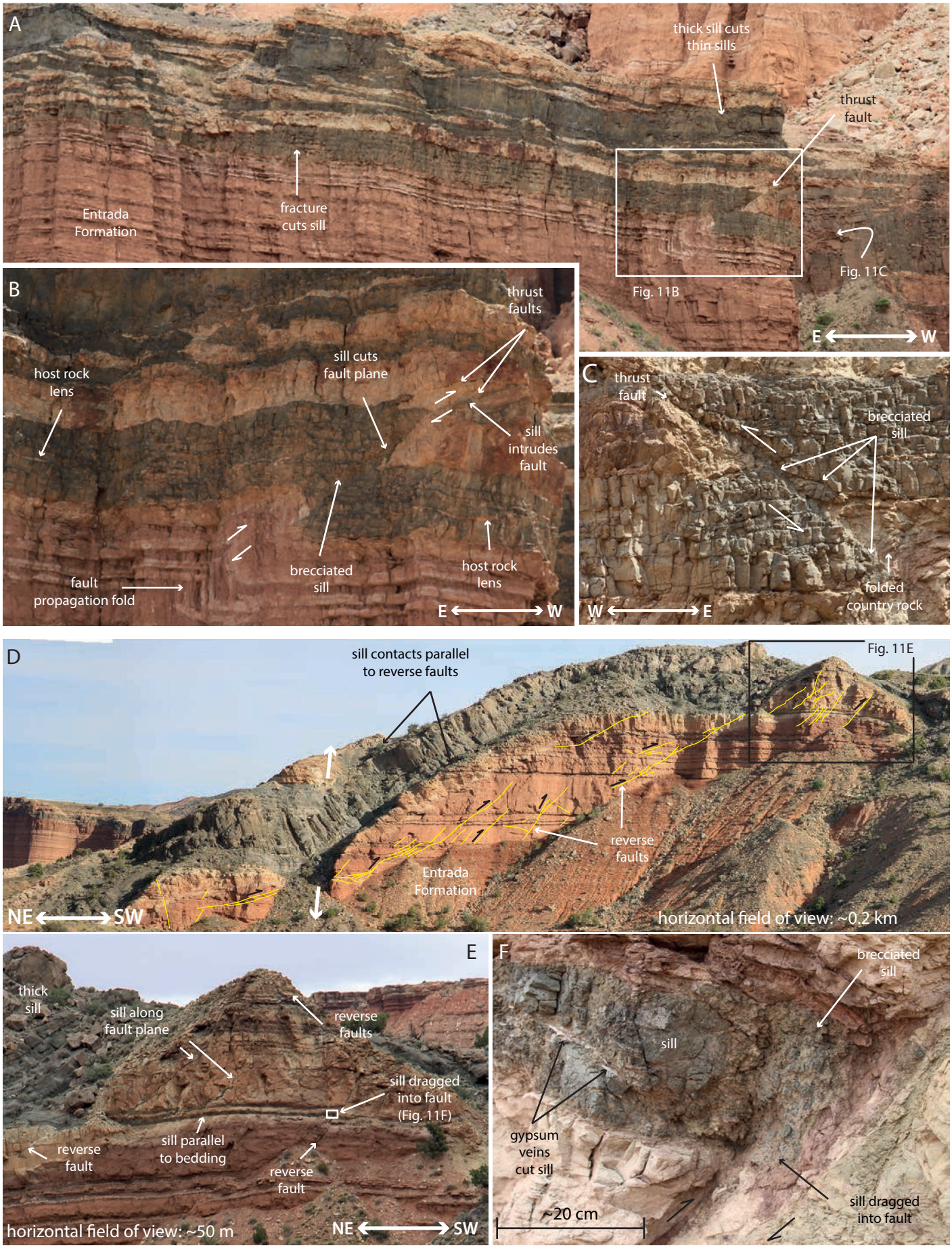

Fig. 11
continued
(full page width)

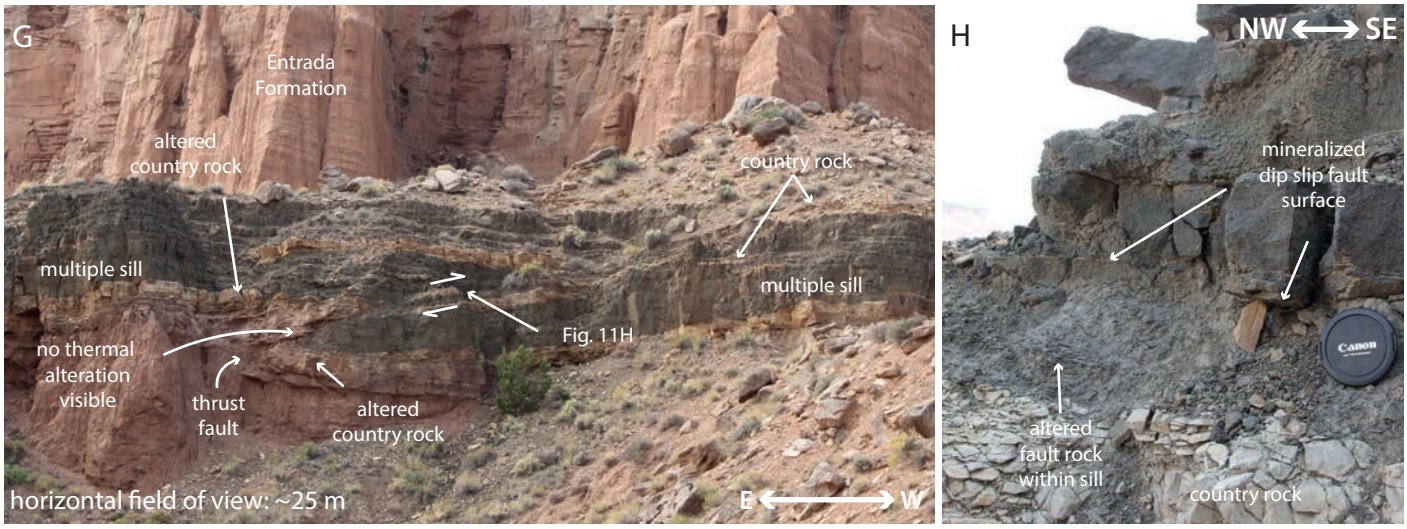

Fig. 11. Relationship between sills and reverse faults. (A-C) Sills cut and are cut by a thrust fault. (B) A multiple sill is cut by an E-dipping thrust. In the upper right of the image, a separate thin sill is observed along the fault plane, inferred as representing post fault intrusion. (C) View from the other side of the crag shown in A and B. Minor fractures parallel to the thrust are observed in the multiple sill. Breccia of the sill is developed along the main thrust, and along minor faults that are sub-parallel to it. (D-F) A thick sill that shows a ramp-flat-ramp geometry, parallel to reverse faults (dipping 25-45° NE) within the country rock. (E-F) Inclined sills appear to have intruded parallel to thrusts, suggesting they reactivate existing structure, but are also locally cut by thrusts. (F) Bedding-parallel sill is dragged into a reverse fault. The sill hosts gypsum-mineralized fractures. Fault rock along the reverse fault comprises breccia of the country rock and the sill. (G) Multiple sill appears to be offset across a thrust fault (dipping ~10°E). Note that the country rock in contact with the sill displays thermal alteration, with the exception of the zone along the thrust plane. (H) Along the fault plane, the sill displays mineralized dip slip fault surfaces, and a 5-10 cm thick zone of altered fault rock.

Fig. 12
W: 123 mm
H: 64 mm
(2-column width)

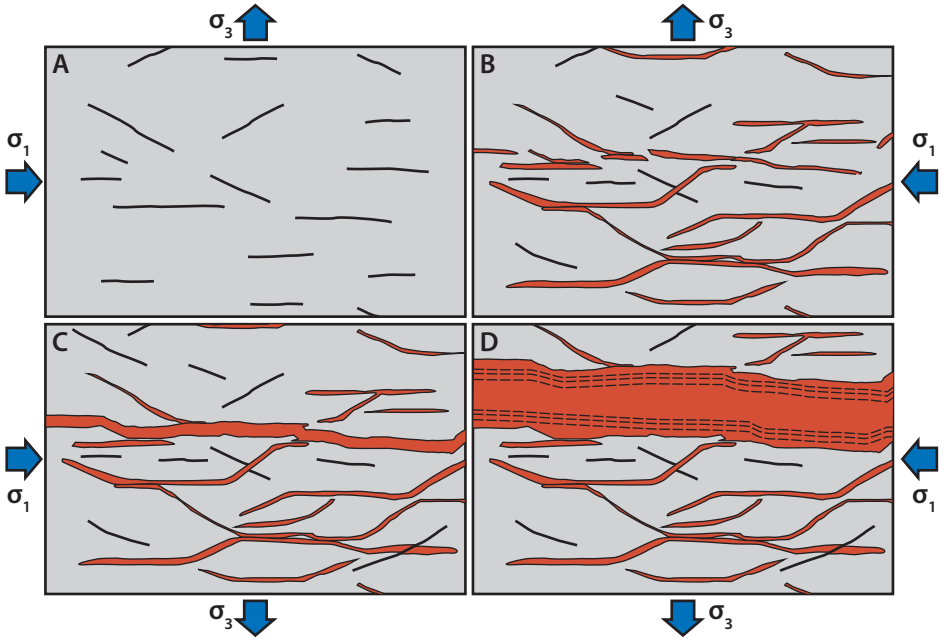

Fig. 12. Conceptual model for sill emplacement during compression. (A) Horizontal shortening produces a fault and fracture system comprising isolated inclined and flat segments. (B) Existing fractures are infilled and inflated by magma and propagate as extension and extensional shear veins. (C) Adjacent sheets link to form a through-going sill. New fractures and faults continue to form during ongoing compression. (D) Minor sills are abandoned in favour of the more thermally -efficient main sill. Note that, as this process may operate across scales, the illustrated box widths may represent centimetres to hundreds of metres, provided there is fault/fracture connectivity in or out of the page.

Fig. 13
W: 123 mm
H: 119 mm
(2-column width)

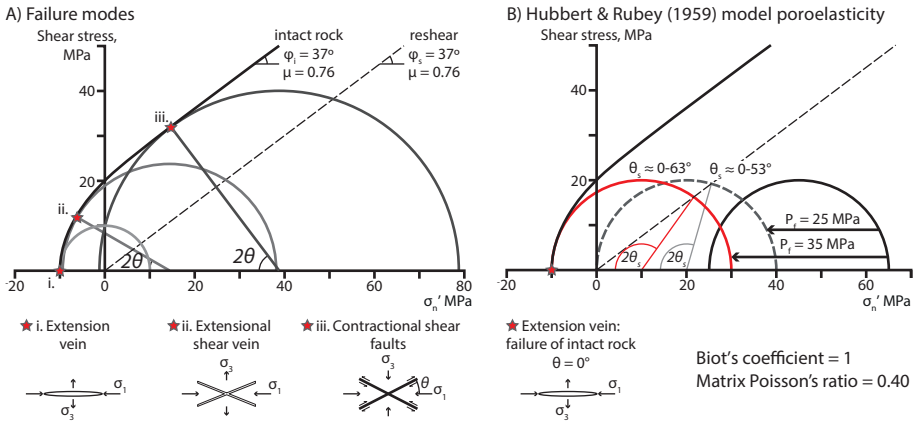

Fig. 13. Mohr diagrams depicting the poroelastic response to isotropic pores and oriented cracks, and to different values of host rock Poisson's ratio. (A) Example Mohr diagram (shear stress, τ, against normal stress, σ) showing the composite failure envelope for intact rock (solid black line) plus the reshear condition for a cohesionless fault (dashed black line), and critical stress circles for the three mesoscopic modes of failure. Diagrams are symmetric about the abscissa, hence the diagrams are simplified to the upper half here. θ represents the angle between the failure plane and the σ1 axis; θs denotes the angular range where reactivation is possible; μ is the coefficient of friction; ϕi is the angle of internal friction for intact rock; ϕs is the angle of internal friction for reshear of a cohesionless fault. Values are idealised based on the Berea sandstone (Healy, 2012). (B) The classical model for the application of fluid pressure (P_f) (after Hubbert and Rubey, 1959). The model involves idealised values for rock compressibility (i.e. Poisson's ratio) and Biot's coefficient, so that the applied fluid pressure has a 1:1 influence on the normal stress.

Fig. 14
W: 123 mm
H: 51 mm
(2-column width)

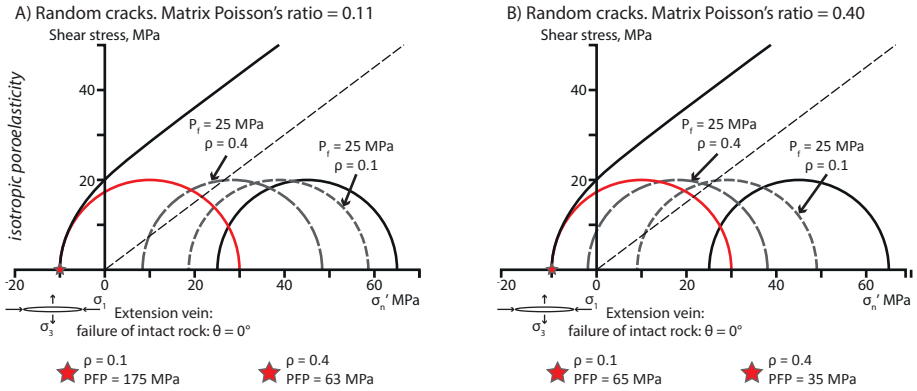

Fig. 14. Mohr diagrams illustrating the poroelastic effect of crack density, and Poisson's ratio at (A) 0.11, and (B) 0.4. Cracks in the model are randomly oriented (i.e. isotropic). Black circles are the normal stress before fluid pressure is applied; grey short-dashed circle shows the effect of 25 MPa fluid pressure where ρ = 0.1; grey long dashed lines circle shows the effect of 25 MPa fluid pressure where ρ = 0.4; red circle shows failure condition.

Fig. 15
W: 123 mm
H: 120 mm
(2-column width)

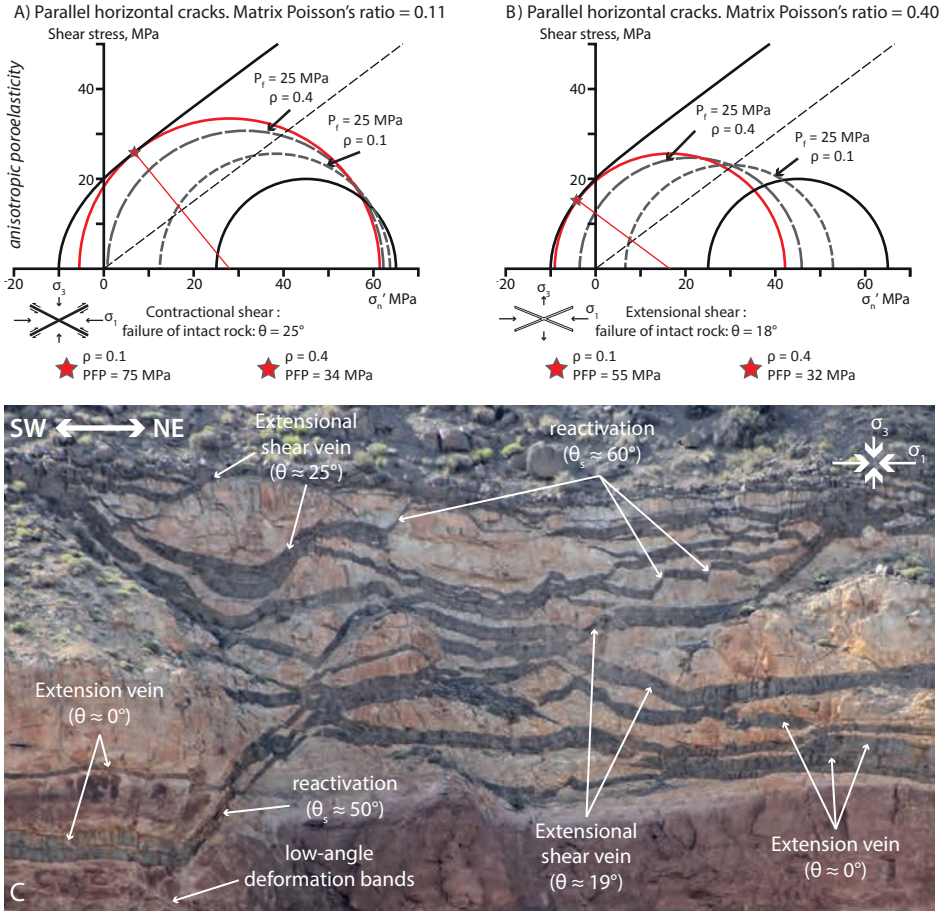

Fig. 15. Mohr diagrams illustrating the poroelastic effect of anisotropic crack density, and Poisson's ratio at (A) 0.11, and (B) 0.4. Cracks in the models are horizontal. Black circles are the normal stress before fluid pressure is applied; grey short-dashed circle shows the effect of 25 MPa fluid pressure where ρ = 0.1; grey long dashed lines circle shows the effect of 25 MPa fluid pressure where ρ = 0.4; red circle shows failure condition. (C) Photograph shows example of sills in the southern SRSVF, highlighting the range of sill attitudes observed in the field. Notably the extension direction is ubiquitously vertical, parallel to our inferred σ_3 axis.